Chapter 5
Metal Abundances in the Hot ISM of Elliptical Galaxies

Dong-Woo Kim

Abstract X-ray spectroscopy provides a powerful tool to measure various elemental abundances in the hot ISM and the measured abundances in turn can be compared with galaxy chemical evolution models to constrain important astrophysical quantities and to help our understanding of the formation and evolution of elliptical galaxies and their ISM. In this chapter, I will address various technical issues involved in X-ray spectral fitting and review observational results of metal abundances in the hot ISM of elliptical galaxies.

5.1 Introduction

Heavy elements in the hot halos of elliptical galaxies are the relics of stellar evolution. Determining their abundance is key to our understanding of the formation and evolution of these galaxies. In particular, since metal abundances are directly related to the stellar mass loss and supernova (SN) ejecta, they can provide an important clue on the star formation history and constrain the SN rate and the initial mass function (IMF) of the stellar population. In addition to the absolute abundances, the relative abundance ratio, particularly the ratio of Fe to α-element, carries important information on the metal enrichment history of the ISM. Since Fe is primarily produced in SN Type Ia (exploding white dwarfs by mass transfer in close binary systems) and α-elements are produced in SN Type II (core-collapsed massive stars), the abundance ratio directly provides the relative importance of the two types of SNe (see Table 5.3 for SN yields of several important elements). Moreover, spatially resolved thermal and chemical structures are important in understanding the evolution of the hot interstellar medium (ISM) via AGN and

D.-W. Kim (✉)
Harvard-Smithsonian Center for Astrophysics, 60 Garden Street, Cambridge, MA 02138, USA
e-mail: kim@cfa.harvard.edu

D.-W. Kim and S. Pellegrini (eds.), *Hot Interstellar Matter in Elliptical Galaxies*,
Astrophysics and Space Science Library 378, DOI 10.1007/978-1-4614-0580-1_5,

SN feedback, which may cause global (e.g., onset of galactic winds) and local (e.g., buoyantly uplifted cavities) structural variation throughout the ISM evolution. Yet these abundance measurements are difficult, and the results have often been controversial.

Following the standard stellar evolution models of passively evolving elliptical galaxies where heavy elements come out of stellar mass loss and additional SN Ia ejecta, we would expect that the metallicity in the hot ISM is higher than or at least as high as that observed in the stellar system, i.e., super-solar metal abundance (Arimoto et al. 1997). While recent results with Chandra and XMM-Newton data suggest that the extremely low Fe abundances (often reported in earlier missions) can be statistically rejected in X-ray bright, gas-rich elliptical galaxies, the observed Fe abundance is still lower than expected (see Sect. 5.4). Furthermore, for X-ray faint early type galaxies which contain only a small amount of the hot ISM, the metal abundance is controversial and very low abundances are still reported, even with the Chandra and XMM-Newton data. It is critical to accurately assess all uncertainties associated in the abundance measurement.

In this chapter, I will first summarize in Sect. 5.2 the basic ISM properties which are most relevant to the metal abundance (see also Fabbiano in this book and Statler in this book for more details). In Sect. 5.3, I will discuss technical issues and related uncertainties involved in abundance determination by fitting X-ray spectra. In Sect. 5.4, I will review in detail observational results of metal abundances and the abundance ratios and their implications (see also Pipino in this book for theoretical results).

5.2 The Hot ISM

Before we address the metal abundance in the hot ISM, it is necessary to understand the basic properties of the hot ISM, i.e., how much gas is in elliptical galaxies and how the gas is spatially distributed. In particular, these gas properties are important in selecting the most appropriate X-ray emission model to accurately analyze the X-ray spectra. As shown in Sect. 5.3.1, the resulting metal abundance critically depends on the adopted model.

5.2.1 Amount of the Hot ISM

One of the long standing puzzles in the X-ray study of early type galaxies is the two orders of magnitude spread in L_X(total) for a given optical luminosity (e.g., Fabbiano 1989; White and Sarazin 1991; Eskridge et al. 1995; O'Sullivan et al. 2001; Ellis and O'Sullivan 2006). L_X(total) was used as a proxy for the hot gas content of the galaxies and L_B (now L_K is preferred) was used, as a proxy of the stellar luminosity. Several mechanisms have been proposed to account

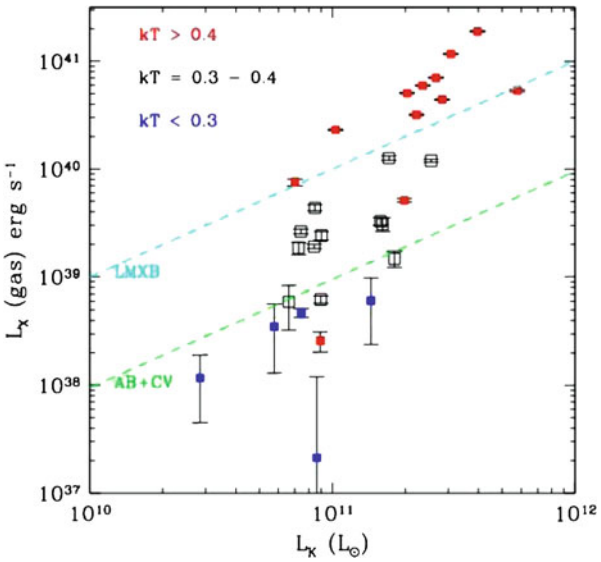

Fig. 5.1 X-ray luminosity of the hot gas is plotted against L_K. Three sub-groups in different kT bins are marked differently (*red, black, blue* in order of decreasing kT). The L_X/L_K ratios corresponding to LMXBs and ABs+CVs are marked by two diagonal lines. Taken from Boroson et al. (2011), reproduced by permission of the AAS

for this spread, including internal (e.g., dark matter, outflow/winds) and external (e.g., ram pressure stripping, infall) effects, but the proper physical process is yet to be explained (e.g., Fabbiano 1989; White and Sarazin 1991). The large $L_X(\text{total})/L_B$ scatter was partly attributed to giant cD-type galaxies filling the high L_X space in the $L_X - L_B$ plane. Since the hot gas dominates the X-ray emission in the gas-rich galaxies with $L_X(\text{gas}) = 10^{41}$–$10^{42}\text{erg s}^{-1}$, $L_X(\text{gas})$ is comparable to $L_X(\text{total})$. However, in gas-poor galaxies, $L_X(\text{total})$ may still be 10^{40}–10^{41}erg s^{-1} because of the stellar contribution, but $L_X(\text{gas})$ is considerably lower than $L_X(\text{total})$: $L_X(\text{gas}) = 10^{38}$–$10^{40}\,\text{erg s}^{-1}$. Therefore the true spread in the $L_X(\text{gas})$–L_K relation is even larger than that of the $L_X(\text{total})$–L_K.

Using a sample of X-ray- (with Chandra observations) and optically- (with optical line measurements) selected elliptical galaxies, Boroson et al. (2011) estimated X-ray luminosities of the hot ISM after properly excluding other emission components, including the nucleus, low-mass X-ray binaries (LMXB), active binaries (AB) and cataclysmic variables (CV). The $L_X(\text{gas})$–L_K diagram is shown in Fig. 5.1. To better represent normal galaxies, their sample does not include a small number of gas-rich cD-type cluster/group dominating galaxies which would reside on the top-right corner (or beyond the range toward the higher L_X) of this plot. The average L_X/L_K relations of a population of LMXBs ($L_X/L_K = 10^{29}\text{erg s}^{-1}L_{K\odot}^{-1}$; see Sect. 5.3.3.1) and ABs + CVs($L_X/L_K = 9.5 \times 10^{27}\text{erg s}^{-1}L_{K\odot}^{-1}$; see Sect. 5.3.3.2) are marked by two diagonal lines in this figure which divide the diagram in three

regions. The number of galaxies in these three regions are roughly the same in this sample which covers a large range in L_X(gas) and L_X(gas)/L_K including both gas-rich, intermediate, and gas-poor galaxies. As seen in Fig. 5.1, the spread is more than 2 orders of magnitude in L_X(gas) for a given L_K($\sim 10^{11} L_{K\odot}$). If we include gas-rich cD galaxies with L_X(gas) $\sim 10^{42}$erg s^{-1} in our sample, the spread in the L_X(gas)–L_K relation would be even larger up to $\sim$3 orders of magnitude. This figure clearly illustrates that there are a number of gas-poor galaxies with a very small amount of the hot ISM, i.e., L_X(gas) is often less than L_X(LMXB) and L_X(gas) may even be less than L_X(AB + CV) in extremely gas-poor galaxies. This also indicates the importance of accurately accounting for the amount of stellar emission (from undetected LMXBs, ABs and CVs as described in Sect. 5.3.3) to determine the gas properties of gas-poor galaxies.

5.2.2 Spatial Distribution of the Hot ISM

Although some spatially resolved features of the hot ISM have been reported in earlier X-ray missions, e.g., X-ray cavity in NGC 1316 (Kim et al. 1998) and X-ray tails in NGC 4406 (Rangarajan et al. 1995), NGC 4472 (Irwin and Sarazin 1996), and NGC 7619 (Trinchieri et al. 1997), it is Chandra which provides unprecedented fine details of morphological and thermal sub-structures of the hot ISM. An excellent example is the multi-phase gas seen in M87, the central galaxy in the Virgo cluster. Million et al. (2010) and Werner et al. (2010) analyzed deep Chandra observations and showed in-depth spatial (see Fig. 5.2) and spectral (see Fig. 5.9 in Sect. 5.4) features. The most striking features are two X-ray arms, which are cooler and have lower entropy (kT $n_e^{-2/3}$) than the surrounding region, and are spatially correlated with the radio emission, strongly indicating that they are likely driven outward by the central AGN. Werner et al. (2010) show that the X-ray arms consist of multiphase medium with gas as cool as 0.5 keV, which spatially coincides with the Hα emission region. Additionally, Million et al. (2010) identified the presence of a thick ($\sim$3 kpc) ring of high pressure gas at a radius of $\sim$14 kpc from the central AGN, which is consistent with an AGN driven shock propagating through the ICM. Several other cavities, shocks, and edges are also seen in the central region (Werner et al. 2010).

Other examples of AGN-related ISM features can be found in cD galaxies, (NGC 5044 by David et al. 2010; NGC 5813 by Randall et al. 2010) and non-cD galaxies (NGC 1316 by Kim and Fabbiano 2003, NGC 4374 by Finoguenov et al. 2008; NGC 4552 by Machacek et al. 2006; NGC 4636 Baldi et al. 2009).

Another type of ISM sub-structures (and not AGN-related) is X-ray tails which are likely being stripped by ram pressure. Clear examples are NGC 4406 (Randall et al. 2008), NGC 4472 (Biller et al. 2004) and NGC 7619 (Kim et al. 2008). In Fig. 5.3, we show the hot gas distribution in NGC 7619, where a long X-ray tail is extended toward the SW. A sharp discontinuity in the opposite direction (NE)

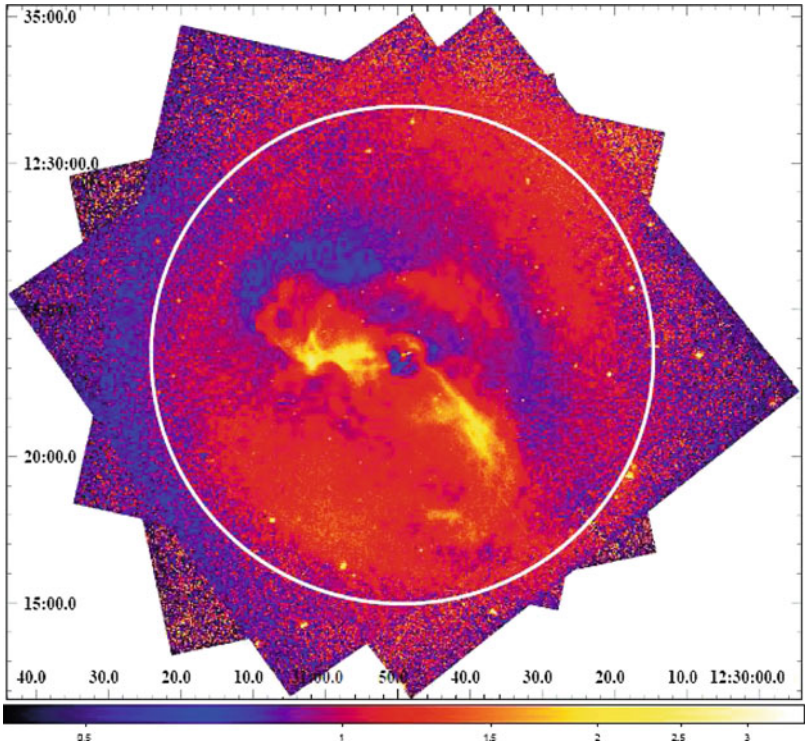

Fig. 5.2 High resolution Chandra image of the central region ($r = 8.6'$ or 40 kpc) of the Virgo cluster, M87. This smoothed surface brightness map was exposure-corrected, flat-fielded and divided by the azimuthally-symmetric double-β model to optimally reveal fine structural details. Taken from Million et al. (2010), reproduced by permission of the RAS

indicates that the galaxy is moving at $\sim$500 km s^{-1} (a Mach number $\sim$1) relative to the surrounding hot gas. Spectral analysis of these data shows that the iron abundance of the hot gaseous medium is much higher (1–2 solar) near the center of NGC 7619 and in the tail extending from the core than in the surrounding regions ($<1/2$ solar), indicating that the gas in the tail originated from the galaxy.

High resolution Chandra observations clearly illustrate complex morphological, thermal and chemical sub-structures of the hot ISM in virtually all gas-rich elliptical galaxies which are either bright enough or close enough for a given Chandra exposure (see by Diehl and Statler 2007, 2008a, b and Statler in this book). As noted above, only a fraction of elliptical galaxies contain a large amount of the hot ISM and were extensively studied for gas sub-structures. If they had been observed in a lower spatial resolution and/or for a shallow exposure, most fine structures might have been missed. If a simplified gas model is applied in X-ray spectral fitting, the measured gas properties could be grossly incorrect, as described below (Sect. 5.3.1).

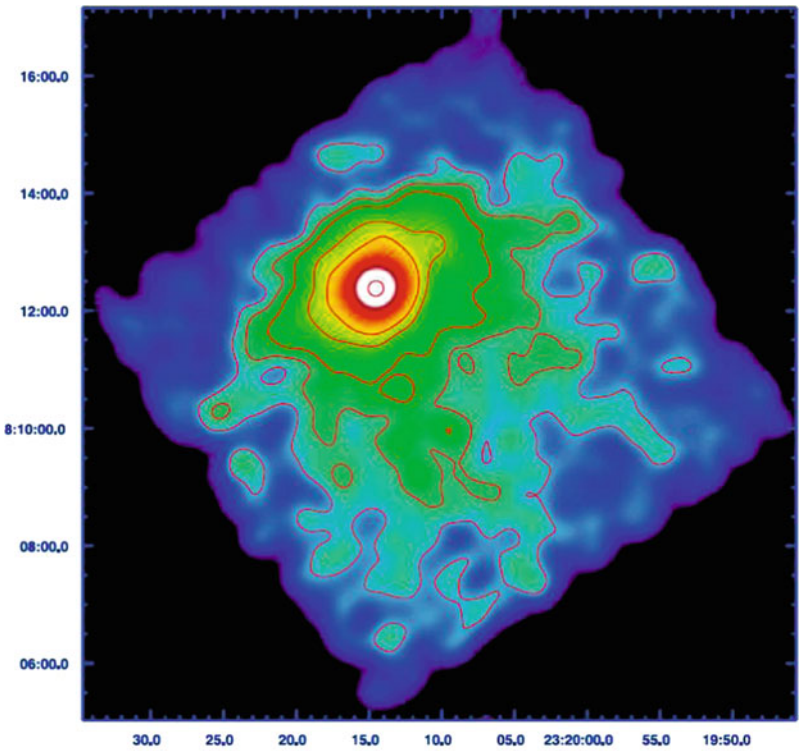

Fig. 5.3 Exposure-corrected, point-source-excluded, Gaussian-smoothed, narrow-band (0.7–1.2 keV) Chandra image of NGC 7619. The X-ray tail extended toward the south-west and the sharp discontinuity in the opposite side are clearly seen. Taken from Kim et al. (2008), reproduced by permission of the AAS

5.3 X-ray Spectral Fitting and Related Issues in Abundance Measurement

Typical X-ray spectra from the gas-rich elliptical galaxies obtained in the current missions are shown in Fig. 5.5 (XMM-Newton MOS), Fig. 5.6 (Chandra ACIS) and Fig. 5.10 (XMM-Newton RGS). As marked in Fig. 5.5, strong emission features from various metal elements are clearly seen in the imaging spectroscopy obtained by the CCD-type instrument.

The emission features consist of multiple emission lines from various transitions. Individual emission lines can be further resolved in the grating spectra, as seen in Fig. 5.10 (see Sect. 5.4.3 for more discussions on grating spectroscopy). Given that the gas temperature in elliptical galaxies ranges from 0.3 keV to 1.2 keV, the strong emission lines are typically from O, Ne, Mg, Si, S and Fe in various ionization stages. In Table 5.1, we list important emission lines from different elements

Table 5.1 X-ray emission lines and peak temperature

Z	Ionization	Stage	E (keV)	λ (Å)	Upper level	Lower level	T_{peak} (keV)
8	O VII	He-like	0.56	22.1	1s2s	$1s^2$	0.2
8	O VII	He-like	0.57	21.6	1s2p	$1s^2$	0.2
8	O VIII	H-like	0.65	19.0	2p	1s	0.3
8	O VIII	H-like	0.78	16.0	3p	1s	0.3
10	Ne IX	He-like	0.91	13.7	1s2s	$1s^2$	0.3
10	Ne IX	He-like	0.92	13.4	1s2p	$1s^2$	0.3
10	Ne X	H-like	1.0	12.1	2P	1s	0.5
12	Mg XI	He-like	1.3	9.3	1s2s	$1s^2$	0.5
12	Mg XI	He-like	1.4	9.2	1s2p	$1s^2$	0.5
12	Mg XII	H-like	1.5	8.4	2p	1s	0.9
14	Si XIII	He-like	1.8	6.7	1s2s	$1s^2$	0.9
14	Si XIII	He-like	1.9	6.6	1s2p	$1s^2$	0.9
14	Si XIV	H-like	2.0	6.2	2p	1s	1.4
16	S XV	He-like	2.4	5.1	1s2s	$1s^2$	1.4
16	S XV	He-like	2.5	5.0	1s2p	$1s^2$	1.4
16	S XVI	H-like	2.6	4.7	2p	1s	2.2
18	Ar XVII	He-like	3.1	4.0	1s2s	$1s^2$	1.7
18	Ar XVII	He-like	3.1	4.0	1s2p	$1s^2$	1.7
18	Ar XVIII	H-like	3.3	3.7	2p	1s	3.4
20	Ca XIX	He-like	3.9	3.2	1s2s	$1s^2$	2.7
20	Ca XIX	He-like	3.9	3.2	1s2p	$1s^2$	2.7
20	Ca XX	H-like	4.1	3.0	2p	1s	4.3
26	Fe XVII	Ne-like	0.73	17.0	$2s^22p^53s$	$2s^22p^6$	0.4
26	Fe XVII	Ne-like	0.83	15.0	$2s^22p^53d$	$2s^22p^6$	0.4
26	Fe XVIII	F-like	0.77	16.0	$2s^22p^43s$	$2s^22p^5$	0.5
26	Fe XVIII	F-like	0.87	14.2	$2s^22p^43d$	$2s^22p^5$	0.7
26	Fe XIX	O-like	0.92	13.5	$2s^22p^33d$	$2s^22p^4$	0.7
26	Fe XX	N-like	0.96	12.8	$2s^22p^23d$	$2s^22p^3$	0.9
26	Fe XXI	C-like	1.0	12.3	$2s^22p3d$	$2s^22p^2$	0.9
28	Ni XIX	Ne-like	0.88	14.1	$2s^22p^53s$	$2s^22p^6$	0.5
28	Ni XIX	Ne-like	1.0	12.4	$2s^22p^53d$	$2s^22p^6$	0.7
28	Ni XX	F-like	0.93	13.3	$2s^22p^43s$	$2s^22p^5$	0.7
28	Ni XX	F-like	1.0	11.8	$2s^22p^43d$	$2s^22p^5$	0.9
28	Ni XXI	O-like	1.0	12.4	$2s^22p^33d$	$2s^22p^4$	0.9
28	Ni XXII	N-like	1.1	11.2	$2s^22p^23d$	$2s^22p^3$	0.9
28	Ni XXIII	C-like	1.2	10.7	$2s^22p3d$	$2s^22p^2$	1.1

in different ionization stages. Also listed are the upper and lower levels (in an abbreviated form without spin and total angular momentum states) and the peak plasma temperatures where a given emission line is strongest. For detail atomic data and line specifications, we refer to the ATOMDB in http://cxc.harvard.edu/atomdb/WebGUIDE) and ASD (atomic spectra database) in http://www.nist.gov/pml/data/asd.cfm.

The strongest feature in the X-ray spectra of the hot ISM is from Fe. The Fe emission features at E = 0.7–1.0 keV (or $\lambda = 12$–17Å) originate from various ionization stages, ranging from Ne-like (with 10 electrons) Fe XVII at low temperatures (kT ∼0.5 keV) to C-like (with 6 electrons) Fe XXI in high temperatures (kT ∼1 keV). The emission features are progressively shifted toward shorter wavelengths (higher energies), as the dominant ionization stages change with increasing temperature (e.g., see Fig. 9.3 in Seward 2000). The ∼7 keV Fe K-shell lines from H-like (with 1 electron) and He-like (with 2 electrons) Fe ions, which are often observed in the hotter ICM (kT = 5–10 keV), are not easily seen in the ISM. The Ne and Ni emission lines are also located at E ∼1 keV and often mixed with stronger Fe emission features. At lower energies (E = 0.5–0.7 keV below Fe features), the O VIII emission lines are strongest and more or less isolated. In contrast, O VII lines, which originate from relatively cooler gas (<0.3 keV), are rarely seen and often used to prove the absence of the cooler gas in cooling flows (see Sect. 5.4.3). The emission features of H-like and He-like Mg, Si, S, Ar and Ca ions are located in a clean part of the X-ray spectrum at E ∼1.5 keV. ∼2 keV, ∼2.5 keV, ∼3 keV and ∼4 keV, respectively (see Fig. 5.5). With increasing ionization potentials (from Mg to Ca), they come from progressively hotter gas.

Ideally, the metal abundances can be measured by fitting proper models to the observed X-ray spectra and the related uncertainties can be constrained by applying proper statistics. Practically, however, there are various systematic effects and simplified assumptions which affect the results but are not easy to fully take into account. In this section, I will review those technical issues and their effects on the measured metal abundances.

5.3.1 Emission Models of Hot Plasma

One of the fundamental problems in abundance measurement is how to select the most appropriate gas emission model. Even though the measured abundances critically depend on the adopted emission model, X-ray spectral fitting often does not statistically require a complex, but realistic model. In this case, investigators tend to stop as soon as the fitting returns reasonable statistics (e.g., χ^2 per degree of freedom ∼1). However, spectral fitting results (particularly the best-fit Fe abundance) can be significantly different when determined, for example, by applying a single-temperature model or a multiple-temperature model. The X-ray spectra of typical hot gas in elliptical galaxies (at kT = 0.3–1.2 keV) peak at E ∼1 keV, mainly by the Fe-L emission feature (see Figs. 5.5 and 5.6; Table 5.1). The peak at E ∼1 keV from mixed gas with two different temperatures (for example, 0.75 keV and 1.5 keV) will be broader than that from isothermal gas at the emission-weighted average temperature (∼1 keV). If the X-ray spectrum from the multi-T gas is fitted with a single-T model, the best fit Fe abundance would be underestimated to reproduce the broad peak (see Fig. 5.4, taken from Buote 2000). This problem is known as *Fe bias* (Buote and Canizares 1994; Trinchieri et al. 1994, 1997; Fabbiano

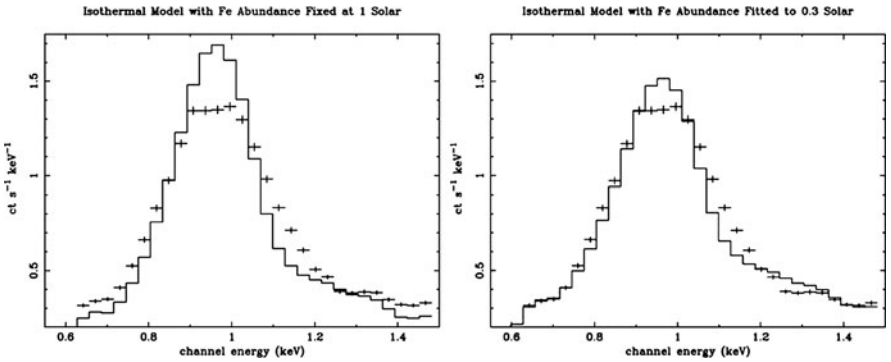

Fig. 5.4 Simulated spectrum (*crosses*) of a two-temperature plasma (0.75 keV and 1.5 keV) with $Z_{\rm Fe} = 1\,{\rm Z}_{\odot}$, and the best-fitting single-temperature model with (*left*) $Z_{\rm Fe}$ fixed at $1\,{\rm Z}_{\odot}$ and (*right*) $Z_{\rm Fe}$ allowed to vary (in this case, the best-fit $Z_{\rm Fe} = 0.3\,{\rm Z}_{\odot}$). Taken from Buote (2000), reproduced by permission of the AAS

et al. 1994; Kim et al. 1996; Buote and Fabian 1998). See more discussion in Sect. 5.4.1.

As described in Sect. 5.2, the hot ISM is likely in multi-phases with multiple temperatures. The multi-phase nature may be caused by a projection effect when the gas temperature distribution is azimuthally symmetric, but has a non-zero radial gradient (see Sect. 5.3.4) or by incomplete mixing of different temperature gas even at the similar radii. A spherically symmetric ISM embedded in spherically symmetric ICM is an example of the former, while mixed gas driven by AGN/SN feedback or by recent mergers may be an example of the latter. The real situation is likely a combination of both effects as in M87 (see Fig. 5.2). It is also important to note the possibility that different phases of ISM may have different metal abundances, but this has not been properly taken into account yet. We will further discuss this problem later.

One of the best examples of multiphase gas is in M87 where Chandra X-ray spectra can be extracted in a small region and analyzed individually due to its high luminosity and proximity (see Fig. 5.2). This spatially resolved spectroscopy reveals the complex spatial distribution of gas temperature and metallicity, related to the AGN activities and mixture of the high metallicity, low temperature ISM and the low metallicity, high temperatures ICM (see Fig. 5.9 in Sect. 5.4 taken from Million et al. 2010; see also Werner et al. 2010). Similarly complex temperature and abundance maps were also reported in NGC 5044 (David et al. 2010). However, this level of spatially resolved spectroscopy is only available in a few gas-rich cD-type galaxies with deep Chandra observations.

Most Chandra and XMM-Newton observations of external galaxies are typically done for a relatively short exposure 20–40 ks. This may still be deep enough for gas-rich galaxies to statistically require a multi-T model. In this case, the Fe abundance is usually close to solar or super-solar (see Sect. 5.4.2). However, for X-ray faint

galaxies with a small amount of hot ISM, the observational data may not statistically require more realistic complex emission models. In this case, a simple 1-temperature thermal plasma model is often applied and, the measured Fe abundance is usually very low (see Sects. 5.4.1 and 5.4.2.3). Ideally, the gas properties can be best measured by spatially resolved spectra. If they are not available, the temperature can still be measured with moderate accuracy from the integrated emission and will be close to the emission-weighted average. However, the abundance cannot be measured that way, because fitting the X-ray spectra from the multi-phase gas with a single temperature model will always return a lower abundance. Therefore, the measured abundance should not be interpreted as an average, e.g., emission-weighted average (for various definitions of average abundances see e.g., Ciotti and Pellegrini 2008; Tang and Wang 2010).

Commonly used hot plasma models are MEKAL (Mewe-Kaastra-Liedahl) and APEC (Astrophysical Plasma Emission Code; Smith et al. 2001). The MEKAL code is based on the model by Mewe et al. (1985, 1986) and Kaastra (1992), and then modified for Fe-L lines by Liedahl et al. (1995). The APEC with atomic database (ATOMDB) provides improved spectral modeling through additional emission lines, accurate wavelengths and new density-dependent calculations. As shown in Sect. 5.3.6, APEC seems to fit the observed spectra better than MEKAL. The detailed comparisons between APEC and MEKAL (e.g., different predictions of O VIII and Fe XVII lines) can be found in the Chandra X-ray Center web site, http://cxc.harvard.edu/atomdb/issues_comparisons.html.

5.3.2 *Absorption Models*

Elliptical galaxies do not contain a large amount of cold gas and dust, as seen in far-IR (e.g., Knapp et al. 1989) and H I observations (e.g., Knapp et al. 1985). With a typical Galactic $N_H(1–5 \times 10^{20}\,cm^{-2}$, away from the Galactic plane), any measureable excess $N_H(> 5 \times 10^{20}\,cm^{-2})$, intrinsic to the target galaxy, corresponds to $M_{HI} \sim 10^9–10^{10} M_\odot$, which is much higher than observed (Knapp et al. 1985). Most recent results obtained with Chandra and XMM-Newton data consistently indicate no extra absorption above the Galactic line of sight H column density (e.g., Kim and Fabbiano 2004; Humphrey and Buote 2006; Ji et al. 2009), although some earlier results with ROSAT and ASCA data did claim intrinsic absorption as much as $N_H \sim 10^{21}\,cm^{-2}$.

If N_H is overestimated, the Fe abundance could be underestimated, by overestimating the continuum level at low energies (e.g., Kim and Fabbiano 2004; Humphrey and Buote 2006). This may also be accompanied by underestimating the hard component from undetected LMXBs (which has the same effect as overestimating the continuum), when fitted with both N_H and the hard component normalization allowed to vary freely. This in turn would affect the continuum both at low ($E < 0:7\,keV$) and high energies ($E > 2\,keV$), reducing the required strength

of the Fe peak at ∼1 keV. This effect was partly responsible for earlier reports of low abundances measured by ASCA and ROSAT data (see Sect. 5.4.1).

Most common absorption models used in the literature are (1) photoelelctric absorption with Wisconsin cross-section (wabs; Morrison and McCammon 1983), (2) photoelectric absorption with a revised cross-section (phabs; Balucinska-Church and McCammon 1992), and (3) Tuebingen-Boulder ISM absorption (tbabs; Wilms et al. 2000) which considers absorption due to the gas, the dust grain and the H_2 molecules. The new version of tbabs (improved in the O K-edge and Fe L-edge) is also available in http://pulsar.sternwarte.uni-erlangen.de/wilms/research/tbabs/. Given that the intrinsic absorption is negligible and that the Galactic line-of-sight N_H is relatively small (a few x 10^{20} cms^{-1}), different absorption models in analyzing CCD spectra do not affect the Fe abundance in any significant manner, as long as the emission and absorption components are properly considered. In general, it is recommended to use tbas with high resolution spectra (e.g., grating data).

5.3.3 Subtraction of Other X-ray Sources

As the metal abundances are basically determined by the line to continuum ratios, it is critical to accurately subtract all non-gas X-ray emission to properly account for the gaseous emission. Incorrect subtraction could affect the continuum level and, in turn, introduce an error in the metal abundance.

5.3.3.1 Low Mass X-ray Binary (LMXB)

Prior to the Chandra mission, individual LMXBs were not easily detected in typical galaxies, mainly due to a poor spatial resolution in the previous missions. The X-ray emission of LMXBs is significantly harder than that of the hot ISM (kT = 0.3–1.0 keV) and well represented either by a Bremsstrahlung model with kT ∼7 keV, or a power-law model with a photon index of Γ ∼1.7 (e.g., Kim et al. 1992; Irwin et al. 2003; Boroson et al. 2011). Because of their harder spectra, the existence of a population of LMXBs could be identified by fitting unresolved spectra, particularly in X-ray faint (gas-poor, LMXB-dominating) galaxies (e.g., Kim et al. 1992), although in some previous studies, the entire X-ray emission was mistakenly attributed to the hot ISM (see Sect. 5.4.1).

With high resolution Chandra observations, most bright LMXBs can be detected and excluded from the diffuse emission. While the problem is generally less critical than before, the remaining population of undetected fainter LMXBs is still important in estimating the gas properties (luminosity, temperature, and metal abundances), particularly for gas-poor galaxies.

5.3.3.2 Active Binary (AB) and Cataclysmic Variable (CV)

Analogous (though less luminous) to LMXBs, active binaries (ABs) and cataclysmic variables (CVs), as seen in the Milky Way (e.g., Charles and Seward 1995), must be properly excluded. The integrated contribution from these sources was identified in M32 and the Galactic bulge (Revnivtsev et al. 2007, 2009), although they cannot be individually detected even with Chandra. They are often ignored because of their relatively small contribution to the total X-ray luminosity, as first estimated by Pellegrini and Fabbiano (1994). However, their contribution to the unresolved emission of the gas-poor galaxies is not negligible, once most bright LMXBs are excluded.

Boroson et al. (2011) characterized the X-ray spectra of a population of ABs and CVs. Their results are similar to those of Revnivtsev et al. (2007), but improved with smaller errors by jointly fitting the Chandra spectra of M31 and M32 with a combination of APEC and power-law (PL) models. They determine the spectral parameters: $kT = 0.48(-0.05, +0.07)$ keV for AP and $\Gamma = 1.76 \pm 0.37$ for PL. The X-ray to K-band luminosity ratio in 0.3 – 8 keV is $L_X/L_K = 9.5^{+2.1}_{-1.1} \times 10^{27}$ erg s^{-1} $L_{K\odot}$ As shown in Fig. 5.1, in extremely gas-poor galaxies (almost 1/3 of their sample), L_X(gas) is less than L_X(AB + CV).

Similar to undetected LMXBs, improper subtraction of the X-ray emission from ABs and CVs would result in incorrect measurements of the hot gas properties. As for the accuracy of metal abundances, the stellar coronal emission (mostly from ABs) will be mixed with the thermal gas emission and the hard emission (mostly from CVs) will affect the continuum level. The previously reported abundance measurements in gas-poor galaxies, if measured without proper consideration of the stellar contribution, need extra cautions (see Sect. 5.4.2.3). In this case, the hard PL component could have been subtracted as a part of a hard LMXB component (although the LMXB emission would have been slightly overestimated), but the soft component would have mistakenly added to the gas emission.

5.3.3.3 Nucleus

In normal early type galaxies, most nuclei are generally weak (so called low-luminosity AGN), when compared to typical AGNs (e.g., Pellegrini 2010), hence the nuclear emission can be isolated and separated from the gaseous emission, as long as the central source is properly excluded in Chandra observations. However, in case of moderately luminous nuclei in some LINERs (e.g., NGC 1052 and NGC 4261; Gonzalez-Martin et al. 2009), extra caution is necessary, because the PSF wing from the nucleus can still affect the emission from the neighboring region and the nuclear emission is often more complex than a simple power-law. Also the AGN may flare up, as seen in NGC 4278 (Cardullo et al. 2009). In this case, the AGN must be fully accounted for to analyze the gas emission in the central region.

5.3.3.4 X-ray Background

The X-ray background consists of the cosmic X-ray background (CXB) and the particle-induced background. The former consists of Galactic diffuse emission, heliospheric and geocoronal diffuse emission and distant AGNs (and possibly warm-hot intergalacitc medium – WHIM). The latter comes from charged/neutral particles (and photons) interacting with detector structures and depositing energy in the instrument. For the nature of the background, we refer to the detailed analyses of the Chandra and XMM-Newton background in http://cxc.harvard.edu/cal/Links/Acis/acis/Cal_prods/bkgrnd/current/ and http://xmm.vilspa.esa.es/external/xmm_sw_cal/background/index.shtml. Here we present how to effectively remove the background emission.

While the background uncertainty has little or no effect for a source which is strong and/or localized in a small region, the accurate background subtraction is critical to analyze an extended diffuse source, like the hot ISM. Ideally, the best way to subtract the background emission from the source emission is to take both at the same detector position at the same time. But this is not feasible in most X-ray observations. Instead, the background is obtained at the source-free region in the same detector (local background), or estimated by properly scaling the pre-made blank sky background template (sky background) which was generated by combining many observations after excluding X-ray sources. Whenever possible, the local background is preferred if the energy-dependent telescope vignetting (decreasing effective area with increasing off-axis angle) is properly corrected.

When the extended source fills up the field of view of the detector, the sky background is the only option. In this case, the background spectra can be extracted from the same detector region as the source spectra. However, the temporal and spatial variations of the background spectra and fluxes need to be corrected. This is often done by screening for background flares and matching source and background count rates at high energies ($>$5–10 keV), where the cosmic background emission dominates over the source emission. This is applicable when the background spectrum does not vary. However, the background may vary in time and space. Furthermore, background X-rays and non-X-ray particles behave differently, e.g., no vignetting for the particle background.

To properly subtract both X-ray and non-X-ray background emission, one may apply more sophisticated, self-consistent method, like the double background subtraction technique described by Arnaud et al. (2002). See also Humphrey and Buote (2006) for a similar technique. After screening the background for flares using the same criteria (i.e., the same count rate at the same energy band) as in the source spectra, applying vignetting correction photon by photon to both the observations and the blank sky background, and scaling the background by the ratio of count rates determined at high energies (e.g., $>$10 keV), the sky background is first subtracted. Then the residual background determined at the source free-region at the edge of the detector is subtracted.

5.3.4 Projection Effect: Spectral Fitting Case 1

To properly extract 3D properties from projected 2D observational data, an onion skin peeling technique is commonly applied. The hot ISM is assumed to be spherically symmetric. This method may be still applicable if the symmetry holds at least within a pie section. In that case, the de-projection can be done within the pie region.

For spectral fitting purposes, it is easier to project the 3D model to the sky plane and then compare with observed spectra extracted from the projected data, rather than de-project the observed spectra. This can be done for example by using a *projct* tool available in the XSPEC package (http://heasarc.gsfc.nasa.gov/docs/xanadu/xspec/), or a *deproject* tool available in the CIAO contributed software (in http://cxc.harvard.edu/contrib/deproject/).

The de-projection effect is most obvious, when the radial gradient is significant, as it also mitigate the problem of the multiphase gas (e.g., Buote 2000; Kim and Fabbiano 2004). Figure 5.5 shows an example of NGC 507 where the gas temperature increases with increasing galacto-centric distance, partly because the cooler (∼0.8 keV) ISM is embedded in a hotter (∼1.4 keV) ambient (ICM) gas (see Sect. 5.4.2 for more details). Because of the temperature gradient, the 3D fitting (upper panels in Fig. 5.5) significantly improves χ^2 statistics over the 2D fitting (lower panels in Fig. 5.5). Also noticeable is the localized deviation in $\Delta\chi$ (excess – deficit – excess around ∼1 keV at the lower panels). This $\Delta\chi$ pattern is likely due to incorrect lines from the same element but in different ionization stages in different temperatures, as described above (see Table 5.1). By properly correcting the projection effect (in the upper panels), not only the overall χ^2 is reduced, but also the local $\Delta\chi$ pattern disappears.

5.3.5 Standard Solar Elemental Abundances

In the last two decades, there have been several different measurements of the solar elemental abundances. They are based on either mass spectroscopy of meteorites or modeling solar photospheric spectral lines, and the results have been significantly different for many key elements (e.g., Fe, O). With considerable improvements in atomic and molecular data as well as in modeling with a realistic time-dependent 3D hydrodynamic model, the photospheric and meteoric abundances seem to converge at least for non-volatile elements (see recent review and redetermination by Asplund et al. 2009). Since volatile elements (H, He, C, N, O, Ne) are depleted in meteorites, they cannot be reliably measured with meteorites.

In Table 5.2, we present three solar standards: two commonly used (ANGR and GRSA) and the most up-to-date (ASPL) standards. Several key elements are listed by number relative to H and Fe. Often in the literature, it is also written in a logarithmic form: for an element X, $\log \varepsilon_X = \log(N_X/N_H) + 12$, where N_X and N_H are the

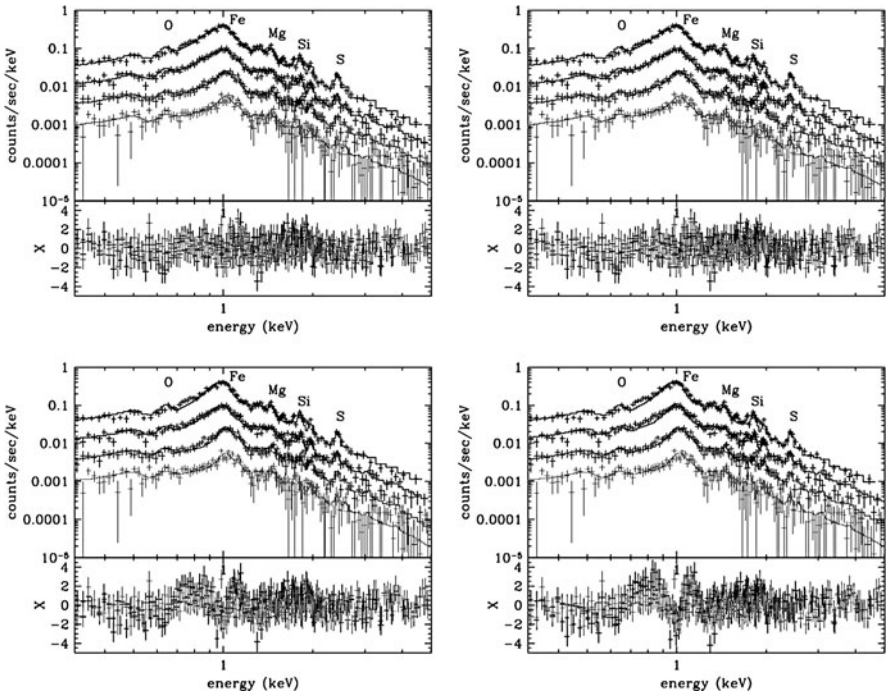

Fig. 5.5 Comparison of spectral fitting in 3D (*top*) and 2D (*bottom*). The *left and right* panels are for 3-component models and 2-component models, respectively. In each figure, the X-ray spectra extracted from r = 0–1′, 1′–2′, 2′–3′ and 3′–5′ are shown from top to bottom. Except for the first spectrum, they are vertically displaced for visibility. Also marked are strong emission features from O, Fe, Mg, Si, and S. The bottom panel indicates the goodness of the fit by $\Delta\chi =$ (observation-model)/error. Note the progressively worse $\Delta\chi$ from the top-left to the bottom-right. Taken from Kim and Fabbiano (2004), reproduced by permission of the AAS

number densities of elements X and H, respectively. For example, $\log \varepsilon_{\rm H} = 12$ and $\log \varepsilon_{\rm Fe} = 7.5$ in ASPL. Another alternative form is [X/H] which is normalized by the solar ratio: for an element X, $[{\rm X/H}] = \log({\rm N_X/N_H}) - \log({\rm N_{X,\odot}/N_{H,\odot}})$. It can be also written in mass: $[{\rm X/H}] = \log({\rm M_X/M_H}) - \log({\rm M_{X,\odot}/M_{H,\odot}})$. In this form, $[{\rm X/H}] = 0.0$ indicates the solar abundance.

Most notably, the Fe abundance was reduced from 4.7×10^{-5} in ANGR (Anders and Grevesse 1989) to 3.16×10^{-5} in GRSA (Grevesse and Sauval 1998) and in ASPL (Asplund et al. 2009). The decrease of the solar Fe abundance by a factor of $\sim$1.5 has somewhat relaxed the Fe discrepancy (described in Sect. 5.4.1). Another notable change is that O, Ne and Ar are significantly reduced. For example, the O abundance decreases from 8.5×10^{-4} in ANGR to 6.8×10^{-4} in GRSA and further decreases to 4.9×10^{-4} in ASPL. Similar to Fe, the change in the O abundance by a factor of 1.7 considerably mitigates the missing O problem (see Sect. 5.4.4.2), although it is still unsolved. The other elements remain almost unchanged.

Table 5.2 Solar element abundances

	By number relative to H			By number relative to Fe		
	ANGR	GRSA	ASPL	ANGR	GRSA	ASPL
O	8.51e-04	6.76e-04	4.90e-04	18.184	21.392	15.506
Ne	1.23e-04	1.20e-04	8.51e-05	2.628	3.797	2.693
Mg	3.80e-05	3.80e-05	3.98e-05	0.812	1.203	1.259
Si	3.55e-05	3.35e-05	3.24e-05	0.759	1.060	1.025
S	1.62e-05	2.14e-05	1.32e-05	0.346	0.677	0.418
Ar	3.63e-06	2.51e-06	2.51e-06	0.078	0.079	0.079
Ca	2.29e-06	2.29e-06	2.19e-06	0.049	0.072	0.069
Fe	4.68e-05	3.16e-05	3.16e-05	1	1	1
Ni	1.78e-06	1.78e-06	1.66e-06	0.038	0.056	0.053

ANGR Anders and Grevesse (1989), *GRSA* Grevesse and Sauval (1998), *ASPL* Asplund et al. (2009)

When comparing abundances reported previously in the literature, it is necessary to rescale for the same solar standard. Note that if O and Fe abundances were solar in ANGR, they would be 1.7 and 1.5 solar in ASPL. The solar O/Fe ratio in ANGR would be non-solar (slightly super-solar) in ASPL. It is also important to note that even after this adjustment the measured abundances may be still affected if different elements are tied in spectral fitting following different solar standards (see Sect. 5.3.6).

While the accuracy in the standard solar elemental abundances has been significantly improved, we should keep in mind that the uncertainties are still far from negligible (see Asplund et al. 2009).

5.3.6 Non-solar Ratios Between Elements: Spectral Fitting Case 2

Another important problem in X-ray spectral fitting is that various element abundances relative to Fe are often fixed at the solar ratio. This practice has been customary mainly because the observed spectra do not have enough statistics to allow variable individual elements. However, some elements are expected to deviate from the solar abundance. For example, the α-element to Fe ratio both in stars and in gas is expected to vary depending on the relative contribution from SN Ia and SN II (see Sect. 5.4.4.1). Also known is the low O abundance (see Sect. 5.4.4.2) relative to Fe and even relative to the same SN II products, Mg (Buote et al. 2003; Kim and Fabbiano 2004; Humphrey and Buote 2006). It is important to note that the measured Fe abundance depends on how other elements are tied. For example, Matsushita et al. (2000) pointed out that the Fe abundance is significantly different when measured with solar and non-solar α-element to Fe ratios. David et al. (2010)

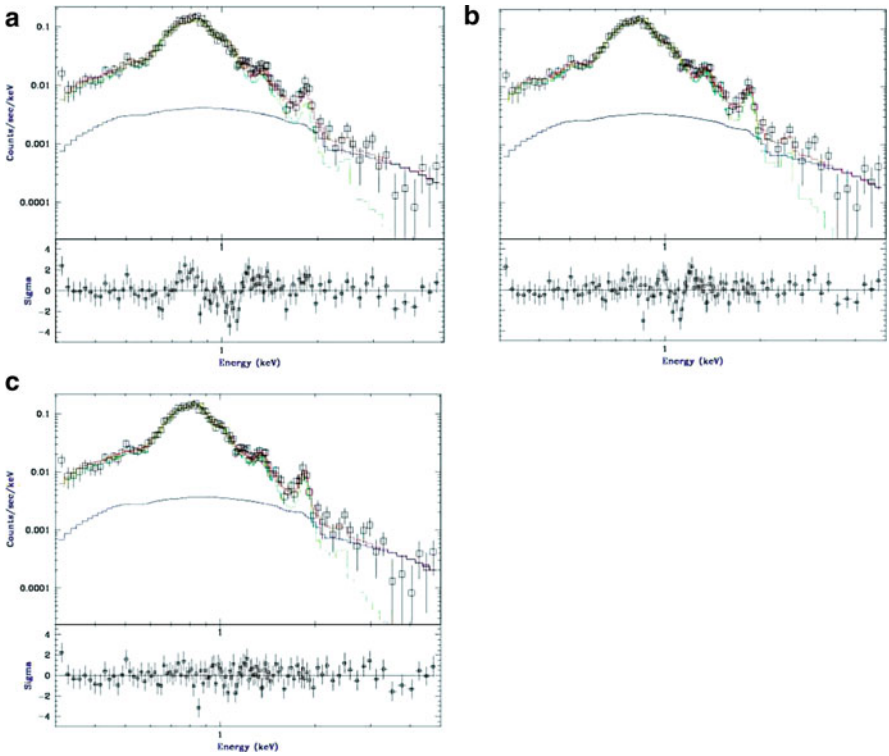

Fig. 5.6 Spectral fitting of Chandra X-ray spectrum extracted from the central ($r < 30''$) region of NGC 720 with (**a**) MEKAL (all elements tied at the solar ratio), (**b**) VMEKAL (all elements allowed to vary independently) and (**c**) VAPEC (all elements allowed to vary independently). Note that the overall $\Delta\chi^2$ (as well as local deviation) is progressively reduced from (**a**) to (**c**), see the electronic version for a color version of this figure

further demonstrated (see their Fig. 5.7) that tying O to Fe results in an incorrect Fe abundance by artificially altering the continuum level at low energies ($\sim$0.5 keV).

To illustrate the effect of tying elements, we compare the spectral fitting results in Fig. 5.6, using deep Chandra observations of NGC 720 (Kim 2010; Kim et al. in preparation). While the hot gas in NGC 720 is extended to $\sim 5'$, the X-ray spectrum was extracted only from the central region ($r < 0.5'$), by separating the outer region which could be in a different temperature and metallicity. This ensures that the simplest emission model (i.e., a single phase gas model) is applicable (Sect. 5.3.1) and that the projection effect is not significant (Sect. 5.3.4) so that the effect of non-solar abundance ratios is best illustrated. Another advantage of using a small region is that the uncertainty in background subtraction is less important (Sect. 5.3.3.4). All detected LMXBs are excluded and a hard component is added for the remaining undetected LMXBs (Sect. 5.3.3.1). Also excluded is an AGN which is relatively weak and its PSF wing does not affect the gas emission (Sect. 5.3.3.3). The X-ray emission from ABs and CVs is negligible in this small region (Sect. 5.3.3.2).

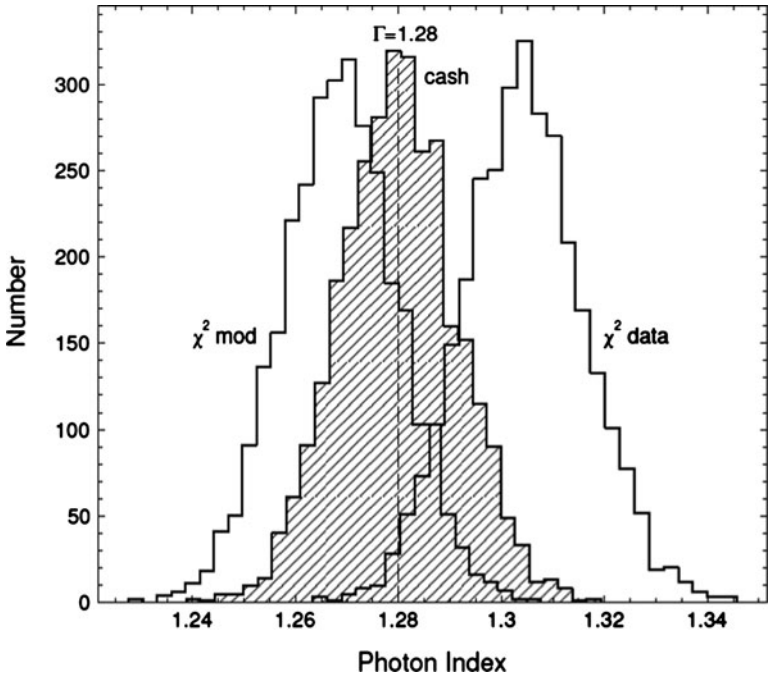

Fig. 5.7 Distributions of a photon index Γ obtained by fitting simulated X-ray spectra with 60,000 counts and using the three different statistics: χ^2 with model variance, χ^2 with data variance and Cash statistics (taken from Siemiginowska 2011)

We fit the X-ray spectrum from the hot ISM in the center of NGC 720 (a) with a 2-component model consisting of MEKAL (all elements relative Fe are fixed at the solar ratio) for the hot gas and 7 keV Bremsstrahlung for undetected LMXBs, (b) by using VMEKAL (instead of MEKAL) with all elements allowed to vary independently and (c) using VAPEC instead of VMEKAL. When all elements are tied (Fig. 5.6a), the metal abundance is statistically constrained at 0.70 (–0.13 +0.19) solar. But the fit is formally unacceptable with the reduced χ^2 of 1.29 for 108 degrees of freedom (dof). A probability that one would observe χ^2 or a larger value is only 0.02. In addition to the poor overall χ^2 statistic, the localized deviations in $\Delta\chi$ (the bottom panel in Fig. 5.6a) are clearly visible near emission features, e.g., excess at 0.5 keV (O), excess at 0.7–0.9 keV (Fe and Ne), deficit at 1.2 keV (Fe), excess at 1.3–1.5 keV (Mg) and excess at 1.8–2.0 keV (Si). This pattern of excess followed by deficit (or deficit followed excess) is similar to that in the lower panel of Fig. 5.5, where the temperature gradient is not properly considered. Since the temperature is relatively well determined and the radial gradient is not important in the small central region, the temperature gradient is not an issue in the center of NGC 720. The problem is likely (1) incorrect individual elemental abundances by arbitrarily tying with other elements, and (2) inaccurate emission models (e.g., in MEKAL and APEC).

When all elements are allowed to vary independently in VMEKAL (Fig. 5.6b), the reduced χ^2 is significantly improved to 1.01 with 96 dof. The fit is formally acceptable with a probability of 0.45. The Fe abundance increases to 1.48 (–0.39 +0.31) solar which is inconsistent ($\sim 2\sigma$ significance) with the first result (0.7 solar). The Si abundance is 2.5 (−0.52 + 0.48) solar which is also inconsistent ($\sim 3\sigma$ significance) with the first results (0.7 solar). While the overall χ^2 was improved to an acceptable level, the localized deviations in $\Delta\chi$ are still visible, most prominently at 0.9–1.3 keV (excess, deficit, then excess).

When VAPEC is used instead of VMEKAL (Fig. 5.6c), the reduced χ^2 is further improved to 0.80 with 97 degrees of freedom, corresponding to a probability of 0.93. Furthermore, no prominent localized deviation in $\Delta\chi^2$ is visible in the entire energy range. Given that the overall statistics and the local deviations significantly improved, VAPEC seems to better represent the hot plasma emission than VMEKAL, as APEC is known to use more accurate plasma emission data (Smith et al. 2001). The Fe and Si abundances are 0.80 (–0.71 + 0.27) and 1.37 (–0.28 + 0.31) solar, respectively. The Si/Fe abundance ratio is 1.71 solar. The Fe and Si abundances are again inconsistent with the MEKAL results ($1–2\sigma$ significance), and also with the VMEKAL results ($1.5–2\sigma$ significance). It is clear that the Fe abundance significantly varies, depending on the way how elements are tied and the adopted plasma model. It is also interesting to note that while the Fe abundance is quite different (1.48 and 0.8 solar in VMEKAL and VAPEC, respectively), the Si/Fe abundance ratio is very similar (1.7 solar in both cases). The relative abundance ratio is often more reliable than the absolute abundance (see Sect. 5.4.4).

5.3.7 Optical Depth for Strong Emission Lines

The ISM is, in general, optically thin and its X-ray spectrum is well represented by an optically thin hot plasma model (e.g., APEC). However, the resonance scattering of the strongest line may not be negligible in a high density environment. In that case, the ISM is no longer optically thin for that line. The resonance scattering can also provide important information about the turbulent velocity in the hot plasma, as it depends on the small scale gas motion (Werner et al. 2009).

The resonance scattering was identified for a strong Fe XVII line at 15Å (see Table 5.1) in the core of NGC 4636 by Xu et al. (2002) and confirmed by Werner et al. (2009). Analyzing the RGS spectra of NGC 4636, Xu et al. (2002) showed that the ratio of the weaker Fe XVII 17Å line to the stronger 15Å line (see Table 5.1) peaks at the center of the galaxy and decreases with increasing projected distance, as expected when the strong Fe line at 15 Å is being suppressed at the center by resonant scattering. Werner et al. (2009) further studied five gas-rich elliptical galaxies and found the resonant scattering effect in the cores of four galaxies (NGC 1404, 4472, 4636, 5813) and estimated that correcting for this optical depth effect increases Fe and O abundances by 10–20%. By excluding the problematic line at

15Å in their spectral fitting, Ji et al. (2009) found that the correction of resonant scattering increases the Fe abundance by 20–30% in NGC 4636. However, they found no change in other gas-rich galaxies including NGC 4472 where Werner et al. (2009) found the suppressed Fe XVII line at 15.01Å.

5.3.8 Helium Sedimentation

The Helium abundance cannot be determined by X-ray spectral fitting and is usually assumed to be solar. However, if the He abundance is enhanced, other element abundances will be reduced due to over-estimating Bremsstrahlung continuum emission. The enhanced He abundance could occur due to the diffusion under the gravitational potential at the center, known as helium sedimentation (e.g., Fabian and Pringle 1977; Gilfanov and Syunyaev 1984). Considering relaxed galaxy clusters, Ettori and Fabian (2006) showed that a He enhancement by a factor of a few with respect to the solar value could reduce by ∼50% the metallicity measured in the center of the ICM (while it does not change the gas temperature) and might explain the metallicity drop reported in the inner (∼20 kpc) regions of nearby bright galaxy clusters (e.g. Centaurus et al. 2002; A2199, Johnstone et al. 2002). The metallicity drop was also seen in galaxy groups with gas in a lower temperature (1–2 keV) (e.g., Rasmussen and Ponman 2009) which, if proved, may be caused by the same effect (however, there may be a problem in this measurement, as described in Sect. 5.4.5). Additionally, the enhanced Far UV flux (called UV upturn) often found in the bright cluster galaxies may be explained by the helium sedimentation due to He-enhanced core-He burning HB (horizontal branch) stars (Peng and Nagai 2009). However, the sedimentation rate could be significantly reduced by the presence of magnetic fields, which is not well understood. The effect of the He sedimentation on reducing measured metal abundances may be somewhat different in the ISM at a lower temperature (∼1 keV or less) and a lower density, as the drift velocity depends on them, $v_D \sim T^{3/2}\, n^{-1}$ (Fabian and Pringle 1977). It is necessary to properly calculate the amount and time scale of the He diffusion under the galaxy environment.

5.3.9 Calibration Uncertainty

The relative calibration uncertainties between different instruments can be measured and possibly corrected by comparing data taken by multiple instruments. However, most cross-calibration studies indicate that systematic differences still remain between different missions and even between different instruments onboard the same observatory.

Recently, led by the international working group, IACHEC (International Astronomical Consortium for High Energy Calibration, see http://www.iachec.org/), a

cross-calibration study has been initiated for most current X-ray observatories, including Chandra, XMM-Newton and Suzaku. A few initial results with well known targets (e.g., supernova remnants and clusters of galaxies) have been reported (Plucinski et al. 2008; Nevalainen et al. 2010; Tsujimoto et al. 2010). They identified systematic differences in the best-fit parameter values which cannot be attributable to the statistical scatter of the data alone.

Plucinski et al. (2008) investigated a supernova remnant in SMC, 1E0102.2–7219 to compare O lines (0.57 and 0.65 keV) and Ne lines (0.92 and 1.0 keV – see Table 5.1). They found the maximum discrepancies as high as 13–24% among Chandra, XMM-Newton and Suzaku instruments. Tsujimoto et al. (2010) used another supernova remnant, G21.5–0.9 (also called Pulsar wind nebula) and found that the differences can be as large as 20% and 9% for the 2–8 keV band flux and power-law index, respectively, but could not study softer energies (<2 keV) due to very high absorption.

Nevalainen et al. (2010) used a sample of 11 relaxed clusters of galaxies whose X-ray emission is dominated by optically thin ionized plasma emission at kT = 2.5–9 keV. They measured the energy dependent effective area by comparing the temperature measured with different instruments and the normalization of the effective area by comparing the flux. While the temperatures agree well when determined in the hard band (2–7 keV), they disagree when measured in the soft band (0.5–2 keV), the ACIS temperature being ∼18% higher than the PN temperature. In the full band (0.5–7.0 keV), the temperatures measured with the EPIC or ACIS data are uncertain by ∼10–15% on average. While the fluxes agree relatively well in the soft band, there is a significant systematic difference in the hard band, the ACIS flux being ∼ 11% higher than the PN flux.

In addition to the cross-calibration uncertainties between observatories, there are important calibration issues related to the time-dependent instrument responses in the same observatory. For example, the Chandra ACIS instrument is known to suffer from molecular contamination which has been building up on the optical blocking filters (see http://cxc.harvard.edu/cal/memos/contam_memo.pdf). This causes the ACIS QE (quantum efficiency), hence ARF (auxiliary response function), to vary in time (also in energy, and detector position). Therefore, it is necessary to take into account the QE difference when compare two ACIS observations taken in different times.

The cross-calibration uncertainties are on the order of 10–20%. However, it is not straightforward to translate these results to the uncertainties relevant to metal abundances in the hot ISM. The most critical factor for the ISM abundance is the uncertainty of the energy dependent effective area in the soft band (0.5–2 keV) where most important emission features reside and where the characteristics of CCD-based instruments (e.g., QE and spectral resolution) are rapidly changing. This could selectively affect some elements due to localized uncertainties, e.g., calibration uncertainties at the C and Si edges. This could also affect the continuum level determined in different energies (e.g., hard emission from undetected LMXBs determined at higher energies) or in different instruments (e.g., when imaging data are used to analyze grating data in Sect. 5.4.3). It will be necessary to perform

an extensive study with a sample of elliptical galaxies to fully understand the calibration effect on the metal abundance measurement.

5.3.10 Statistics: χ^2 vs. Cash Statistic

Two commonly used statistics are χ^2 and cash (or C-stat). The χ^2 method, most widely used in the literature, can determine both a confidence interval of each parameter and a goodness-of-fit. In this method, the X-ray spectra need to be binned with at least 20–30 counts in each bin to properly apply the Gaussian approximation. On the other hand, the cash statistic (Cash 1979) can be applied regardless of the number in each bin. However, a goodness-of-fit measure is not assigned to a given value of the cash statistic and Monte Carlo simulations are required.

In the χ^2 statistic, the variance is calculated from the data (called data variance) by simply taking $\sqrt{N}$, where N is the number of observed counts in a given bin. Alternatively, the variance can be calculated from the model amplitude (called model variance). With a finite number of observed counts, both data and model variances could be biased, called χ^2 *bias* (Siemiginowska 2011; see also Humphrey et al. 2009). This bias is illustrated in Fig. 5.7, taken from Siemiginowska (2011). X-ray spectra of a single power-law model were simulated with Chandra calibration response files and the Poisson noise was added. Then the simulated spectra were fitted with the same model to determine the best fit parameter. The simulation results show that the model-variance χ^2 statistic underestimates the power-law index and the data-variance χ^2 statistic overestimates. Conversely, the cash statistic returns more reliable results (see also Humphrey et al. 2009). Another alternative is to use Gehrels variance function, $1 + \sqrt{N+0.75}$ (Gehrels 1986) to better approximate in the low-counts regime. However, this approximation is too conservative and may overestimate the size of the confidence range for a given significance.

In most practical cases of the hot ISM, the statistical error is larger, and the emission model is more complex than depicted in Fig. 5.7 and additionally various non-negligible systematic errors are complex as described in Sect. 5.3.1–5.3.9. Therefore, this χ^2 bias might not cause a problem in any significant manner in the published results. However, it is important to take into account this bias in analyzing high s/n spectra and also in future missions.

5.4 Observed Metal Abundances in the Hot ISM of Elliptical Galaxies

5.4.1 Before Chandra and XMM-Newton

In early X-ray missions, the observationally measured Fe abundance was often sub-solar and considerably lower than expected. This problem is often referred to as the

Fe discrepancy (e.g., Arimoto et al. 1997; Pipino in this book). It was most serious when poor (spectral and spatial) resolution spectra (like ROSAT and ASCA data) were analyzed by fitting a simplified emission model, e.g., a single temperature (1T) thermal plasma model (sometimes with an additional hard component to take into account LMXBs). As described in Sect. 5.3.1, the reported Fe abundances were always lower than 0.5 solar and quite often as low as 0.1 solar (e.g., Awaki et al. 1994; Loewenstein et al. 1994; Davis and White 1996; Matsumoto et al. 1997). Furthermore, the associated statistical errors (taken directly from the spectral fitting) were usually very small.

It is interesting to note that the metal abundances measured using the X-ray (mostly ASCA) spectra from stellar coronae had suffered from the similar problem of anomalously low metal abundances, Fe abundances as low as 10–30% of the solar value were regularly reported (e.g., see a review by Gudel 2004).

As described in Sect. 5.3.1, the observationally measured Fe abundance critically depends on the adopted model. Analyzing ROSAT data, several investigators (Buote and Canizares 1994; Trinchieri et al. 1994, 1997; Fabbiano et al. 1994; Kim and Fabbiano 1995) recognized that the observed spectra could allow not only a 1-T gas model with very low Z_{Fe}, but also a 2-T gas model with roughly solar Z_{Fe}, although they could not distinguish the two possibilities due to the limited spectral resolution. Kim et al. (1996), using additional ASCA data, could reject the very low abundance 1-T model in NGC 4382. Buote and Fabian (1998) further analyzed ASCA data of 20 gas-rich early type galaxies and confirmed that the extremely low abundance is not required. They found that the Fe abundance is close to solar, when fitted with a 2-T model and that in a few very high S/N galaxies, an even more complex, 3-T model is preferred.

Buote (2000) also pointed the importance of the projection effect to correctly account for the temperature and abundance gradient (see Sect. 5.3.4). Analyzing ROSAT data of 10 galaxies and groups, he found that the Fe abundance decreases with increasing radius: from $Z_{Fe} \sim$ 1- several $Z_\odot$ within the central radial bin ($r <$ 10 kpc) to $Z_{Fe} \sim 0.5 Z_\odot$ at the largest radii examined ($r \sim$50–100 kpc). The negative gradient of the Fe profile was reported earlier, e.g., in NGC 4636 by Mushotzky et al. (1994), but the absolute abundance was less accurate (sub-solar) in the entire radius range.

Reanalyzing ASCA data of 27 elliptical galaxies, Matsushita et al. (2000) pointed out the effect of coupling among different elements. As discussed in Sect. 5.3.6, the allowed abundances of two elements (e.g., Fe and α–elements) are often strongly coupled such that the confidence contours of two interesting elements are diagonally elongated. Because the continuum level might be raised or lowered by incorrectly tying different elements, the measured Fe abundance would change with non-solar Fe to α ratios. Matsushita et al. (2000) found that the metallicity becomes significantly higher with a non-solar α to Fe ratio than with the fixed solar ratio (also by adding a systematic error of ∼20%) and becomes close to $\sim 1 Z_\odot$ within a factor 2.

5.4.2 The Chandra and XMM-Newton Era

5.4.2.1 Gas-Rich cD Galaxies

Taking advantage of high spatial resolution in Chandra and a large effective area in XMM-Newton, many investigators have revisited the low metal abundance problem. The new results generally suggest that extremely low, sub-solar, Fe abundances can be statistically rejected at least in X-ray bright elliptical galaxies (this section and Sect. 5.4.2.2), although it is still not clear in the X-ray faint, gas-poor galaxies (see Sect. 5.4.2.3 below).

Analyzing XMM-Newton data of NGC 1399, the brightest elliptical galaxy in the Fornax group, Buote (2002) reported that the hot gas is best represented by a two-phase model with T $\sim$ 0.9 keV and $\sim$ 1.5 keV. The lower temperature is comparable to the stellar kinetic temperature and the higher temperature corresponds to a larger scale gravitational mass of $10^{13} M_{\odot}$ associated with the group. The two-phase model returns $Z_{Fe} = 1.5$–$2\ Z_{\odot}$ in the central region ($r < 20$ kpc). At larger radii, the iron abundance drops to $Z_{Fe} \sim 0.5 Z_{\odot}$ at $r \sim 50$ kpc. Similarly analyzing Chandra and XMM-Newton data of NGC 5044, another dominant galaxy in a small group, Buote et al. (2003a, b) reported that the hot gas is well fitted by a two-temperature model with 0.7 keV and 1.4 keV. In this model, $Z_{Fe} \sim 1 Z_{\odot}$ in the central region ($r < 50$ kpc) and $Z_{Fe} \sim 0.4 Z_{\odot}$ at $r = 100$ kpc.

Kim and Fabbiano (2004) analyzed XMM-Newton data of NGC 507, another X-ray bright, dominant elliptical galaxy in a galaxy group. Taking into account various possible systematic effects in their measurement, they clearly reported super-solar Fe (and super-solar α-element) abundance: $Z_{Fe} = 2$–$3 Z_{\odot}$ inside the D_{25} ellipse of NGC 507 (see Fig. 5.8), the highest Z_{Fe} reported for the hot halo of an elliptical galaxy. This high Fe abundance may be still lower than expected, but much closer to the predictions of standard stellar evolution models with the contributions from both SN Ia and SN II.

Similar to NGC 1399 and NGC 5044, the hot ISM of NGC 507 has temperatures ranging from 0.6 to 1.4 keV (within each concentric shell). All three galaxies clearly demonstrate that abundance measurements are critically dependent on the selection of the proper emission model (Sect. 5.3.1). The XMM-Newton and Chandra spectra provide enough statistics to formally require at least three emission components in each concentric shell. In addition to a harder component for the integrated output of LMXBs, two soft thermal components (with relative contribution varying at different radii) are necessary to represent a range of temperatures in the hot ISM. It is important to note that the 3-component model is still an approximation, unless the multiple gas phases are fully resolved (e.g., as in M87 as described below). With a single-phase gas model (with or without the LMXB component) customarily used in the past, both studies (Buote et al. and Kim and Fabbiano) could reproduce a much lower Z_{Fe}, consistent with previous reports of sub-solar metal abundances, but with a large χ^2 value (i.e., statistically unacceptable).

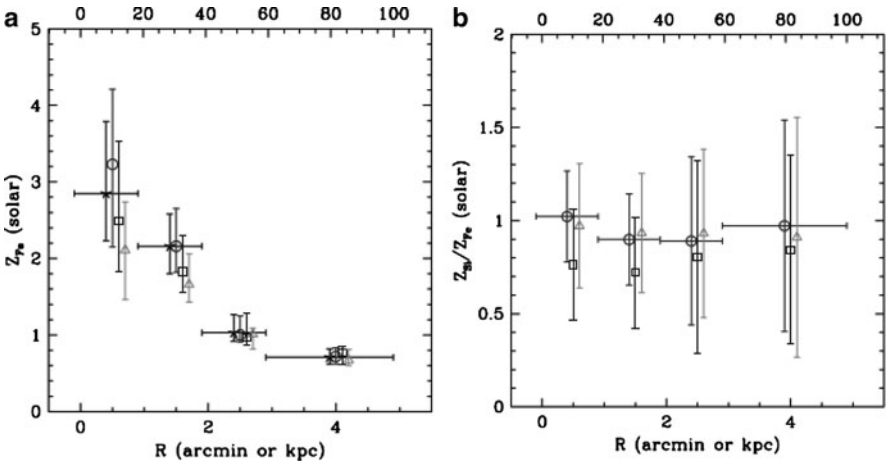

Fig. 5.8 Radial distributions of (**a**) Fe abundances and (**b**) Si-to-Fe abundance ratios measured with Chandra data of NGC 507. Different symbols indicate different ways of tying elements. Taken from Kim and Fabbiano (2004), reproduced by permission of the AAS

The α element abundances (mainly determined by Si) are also close to solar in all 3 galaxies: $Z_{\rm Si}/Z_{\rm Fe} \sim 0.8$ in NGC 1399, $Z_{\rm Si}/Z_{\rm Fe} \sim 0.83 \pm 0.1$ in NGC 5044 and $Z_{\rm Si}/Z_{\rm Fe} \sim 0.8$–1.1 in NGC 507 (see Fig. 5.8). These Fe to Si abundance ratios imply that ∼70% of the Fe mass originates from SN Ia (see Sect. 5.4.4). While the Fe and α-element abundances decrease with increasing radius, their ratio remains constant at the solar ratio over the entire region (out to 100 kpc), indicating that SN II and SN Ia ejecta are well mixed on a scale much larger than the extent of the stellar body (see Sect. 5.4.5).

Recently, spatially resolved high quality spectra are obtained for a few X-ray bright, nearby cD galaxies with ultra deep Chandra observations. Figure 5.2 shows an ultra deep Chandra observation of M87 (total exposure of ∼570 ks). Million et al. (2010) extracted X-ray spectra applying a contour binning method from a small region consisting of neighboring pixels of similar surface brightness, but with enough counts for proper spectral fitting (∼2,500 counts on average in ∼6,000 regions). The spatially resolved spectroscopy reveals in detail the complex spatial distribution of gas temperature and metallicity (see Fig. 5.9 taken from Million et al. 2010; see also Werner et al. 2010). The gas temperature ranges from 0.8 to 3 keV, generally cooler inside (and in the X-ray arms) and hotter in the outskirts, as the ICM contributes progressively more with increasing distance from the center. The metallicity ranges from 0.4 solar to 2 solar, generally higher in the inner region and lower in the outskirts, again by more contribution from the low-metallicity ICM with increasing distance. In addition to the global radial variation, multi-phase gas (with different temperature and metallicity) co-exists locally. Furthermore, in Fig. 5.9, various thermal and chemical sub-structures are seen, e.g., a high metallicity structure is observed at a radius of r ∼4.5 arcmin to the west of the central

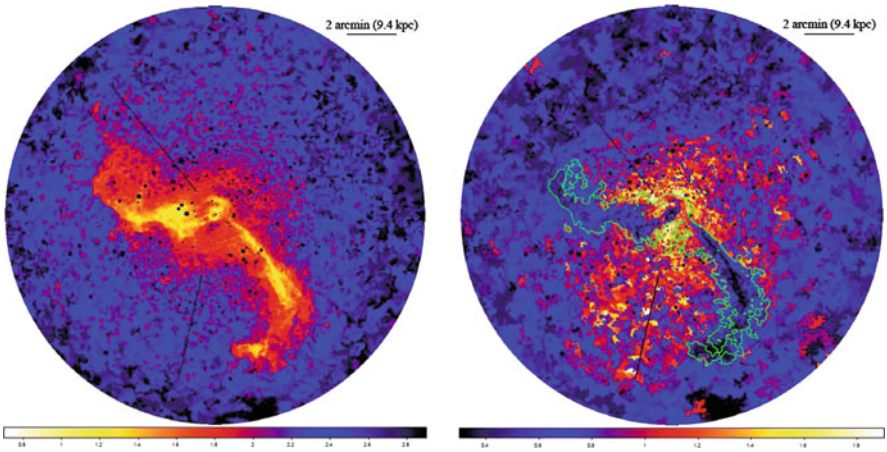

Fig. 5.9 (*top*) Temperature map of the central region of the Virgo cluster (in units of keV). Point sources and readout errors have been excluded (*black holes*). (*bottom*) Metallicity map in solar units. Regions inside the green contours cannot be modeled by a single-temperature plasma and the abundance is significantly underestimated. Taken from Million et al. (2010), reproduced by permission of the RAS, see the electronic version for a color version of this figure

AGN. This ridge connects with the high metallicity extension to the northwest of the core at a radius of r ∼3.3 arcmin. This structure is likely due to the uplift of cool, metal-rich gas in the wake of buoyantly rising, radio-emitting plasma (see Roediger et al. 2007 for numerical simulations of mixing metal by buoyant bubbles). Also noticeable is an asymmetric feature: the southern region is more metal rich than the north.

David et al. (2009, 2010) reported similarly complex features in NGC 5044, with spatially varying amounts of multiphase gas, by analyzing spatially resolved spectra extracted from deep Chandra observations.

While it is clear that the high spatial-resolution spectroscopy is most desirable to properly identify the fine details of the ISM and to measure the gas properties (including metal abundances), this level of detail observational information is only available in a small number of gas-rich nearby cD-type galaxies with deep Chandra observations.

5.4.2.2 Gas-Rich Normal (Non-cD) Galaxies

Humphrey and Buote (2006) re-analyzed archival Chandra data of 28 early-type galaxies, covering a wide range in the X-ray luminosity. In a high-L_X sub-sample ($L_X = 10^{41.5–43}$ erg s^{-1}, including some cD galaxies), the measured Fe abundance is $Z_{Fe} = 0.4–3.0 Z_\odot$, while in a moderate-L_X sub-sample ($L_X = 10^{40.5–41.5}$ erg s^{-1}, all non-cD galaxy), $Z_{Fe} = 0.2–5 Z_\odot$. In their sample, even if the best fit Z_{Fe} is very low, the corresponding error is large such that $Z_{Fe} \sim 1 Z_\odot$ is usually allowed within

the error. They also found no clear difference in Z_{Fe} between high and moderate L_X sub-samples. More specifically, there is no correlation between Z_{Fe} and L_X, possibly indicating that the solar or super-solar Z_{Fe} found in cD galaxies still holds in non-cD normal galaxies with lower L_X.

Ji et al. (2009) re-analyzed archival XMM-Newton EPIC and RGS data for 10 nearby X-ray bright galaxies including two cD galaxies. In their two-phase model fitting, they found $Z_{Fe} = 0.5–1.8 Z_\odot$ with a median Fe abundance of $0.86\ Z_\odot$. Again, there is no Z_{Fe} dependency on the X-ray luminosity.

Both studies indicate that the Fe abundance is generally close to solar in most gas-rich elliptical galaxies and the very sub-solar Fe abundance reported earlier (in Sect. 5.4.1) is statistically rejected. In this regard, cD and non-cD elliptical galaxies do not differ, except that cD galaxies are more luminous and can be investigated in detail.

While the above general trend is obvious, the individual abundance in each galaxy still varies from one measurement to another, often by more than the statistical error. For example, two (NGC 1399 and NGC 4552) of five galaxies which are common in Humphrey and Buote (2006) and Ji et al. (2009) samples have quite different Fe abundances. The reported abundances are sometimes different even when measured by the same instrument and the same model, e.g., with XMM-Newton EPIC data of NGC 4649 (a gas-rich Virgo elliptical galaxy), $Z_{Fe} = 1.4–1.6 Z_\odot$ (for 1T) and 1.6–1.7 $Z_\odot$ (for 2T) by Ji et al. (2009) while $Z_{Fe} = 0.7 Z_\odot$(for 1T) and 1.1 $Z_\odot$(for 2T with all elements tied) by Randall et al. (2006). The quoted error is relatively small ($\sim$0.1 $Z_\odot$). Also note that a low Fe abundance is reported for a gas-rich galaxy even recently, although rare, e.g., in NGC 6251 with 1T gas + power-law (Sambruna et al. 2004). While the sample-averaged metal abundance seems to be reliable, an individual abundance measurement should be taken with caution.

5.4.2.3 Gas-Poor Galaxies

While extremely low, sub-solar, Fe abundances can be statistically rejected in X-ray bright elliptical galaxies (with the best fit Fe abundance close to solar or even super-solar), the measured abundances in X-ray faint, gas-poor, galaxies are still controversial. Very low abundances ($Z_{Fe} < 0.1\ Z_\odot$) are reported from the XMM-Newton data analysis of X-ray faint early type galaxies, for example NGC 3585, NGC 4494, and NGC 5322 by O'Sullivan and Ponman (2004a). Similar low (sub-solar) metal abundances (but with a large uncertainty) were also reported from the analysis of the Chandra data of NGC 4697 (Sarazin et al. 2001), NGC 1553 (Blanton et al. 2001), NGC 1291 (Irwin et al. 2002), NGC 4365 and NGC 4382 (Sivakoff et al. 2003), and NGC 4555 (O'Sullivan and Ponman 2004b).

Is this because the gas metallicity is really lower in gas-poor galaxies than in gas-rich galaxies? Given that the ISM in gas-poor and gas-rich galaxies will be in different dynamical states, outflow/wind vs. inflow (e.g., Ciotti et al. 1991; Loewenstein and Mathews 1991; see also Pellegrini in this book), the metallicity

may be also different. However, it is expected that the ISM metallicity is at least as high as the stellar metallicity. We refer to Pipino (in this book) for possible solutions of this issue. In particular, the incomplete mixing of the SN Ia ejecta suggested by Tang and Wang (2010) may be more effective in the gas-poor galaxies with the lower density outflow/wind state than the gas-rich (higher density) galaxies. Or is this because we do not see the complexity due to a low s/n ratio of gas-poor galaxies? If so, the problem would be similar to the early results of extremely low metallicity reported in the pre-Chandra missions (Sect. 5.4.1). Due to the model-dependency, the measured metal abundance would be lower with a very small error if the adopted model is too simple. Most XMM-Newton and Chandra observations of the X-ray faint galaxies for typically short exposures of 20–40 ks do not statistically require complex emission models. Once again, the measured abundance is model-dependent, 1T with low-abundances or 2-T with abundances close to solar abundance. For example, Kim and Fabbiano (2003) find metal abundances in NGC 1316 consistent with solar, but with a large uncertainty (0.25–1.3 $Z_\odot$) by applying a 3-component model to the Chandra data. They noted that $Z_{Fe} \sim 0.1 Z_\odot$ if a 1T model was applied. Among the gas-poor galaxies ($L_X < 10^{40.5}$ erg s^{-1}) studies by Humphrey and Buote (2006), the best fit value of Z_{Fe} appears to be sub-solar, but because the error is poorly constrained, Z_{Fe} comparable to those in gas-rich galaxies is always allowed.

It is also important to note that the contribution from ABs and CVs must be properly considered in gas-poor galaxies. As described in Sects. 5.2.1 and 5.3.3.2, the X-ray luminosity from the entire ISM can be even lower than that of the population of ABs and CVs in a number of gas-poor elliptical galaxies. For example, NGC 3585 and NGC 4697 (among those listed above) have a relatively low L_X(gas), comparable to their L_X(ABs+CVs). As shown by Revnivtsev et al. (2007) and Boroson et al. (2011), the spectra of ABs and CVs can be modeled by 2-components: soft (APEC with kT ~0.5 keV) and hard (power-law with a photon index of 1.7). Since the hard component is similar to the LMXB spectrum, even if ignored, it might have been subtracted as a part of the LMXB component with no effect on abundance measurement. However, it is the soft thermal component which affects not only the amount of the ISM, but also the metal abundance, because this additional component must be added in the spectral fitting. Up to now, this has not been done properly.

5.4.3 High Spectral Resolution Grating Observations

The XMM-Newton reflecting grating spectrometer (RGS) provides significantly higher spectral resolution ($E/\Delta E = 100$–500 in FWHM) than that available by CCD imaging spectrographs (e.g., $E/\Delta E = 20$–50 in XMM-Newton MOS). Compare EPIC MOS spectra in Fig. 5.5 and Chandra ACIS spectra in Fig. 5.6 with the RGS spectrum in Fig. 5.10. Given that Chandra transmission grating instruments (LETG and HETG) are not suitable for extended sources, RGS is a unique high resolution

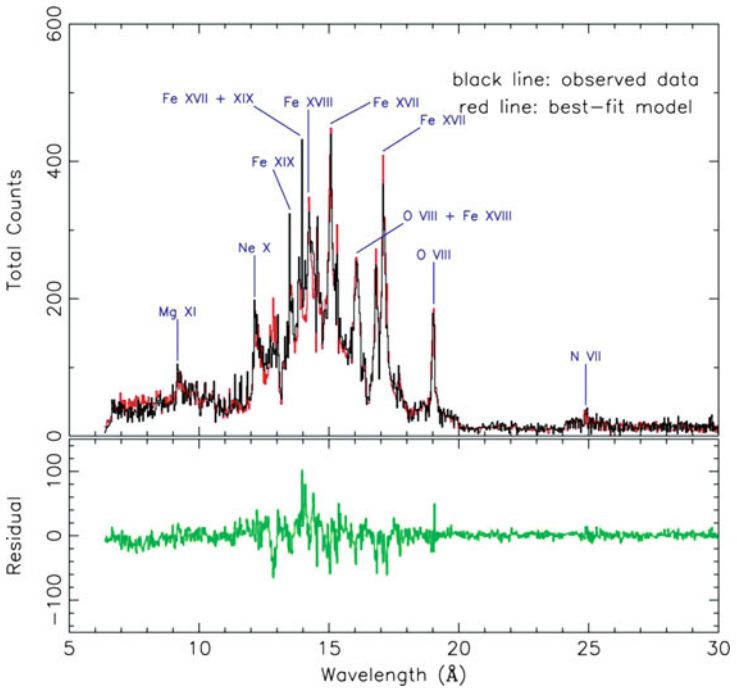

Fig. 5.10 RGS spectrum of NGC 4636 taken from Xu et al. (2002). Both 1st and 2nd order from RGS1 and RGS2 have been added together. Important emission lines from Fe, O, Mg, Ne and N are marked. Reproduced by permission of the AAS, see the electronic version for a color version of this figure

spectrometer which is currently available for X-ray bright galaxies (s/n is too low for X-ray faint galaxies). Analyzing the RGS data of NGC 4636, Xu et al. (2002) showed strong individual lines, such as O VIII, Fe XVII, and Fe XVIII from the hot ISM (Fig. 5.10). See also Ji et al. (2009). Furthermore, Xu et al. (2002) addressed the usefulness of key diagnostic line ratios, such as a temperature-sensitive Fe XVII to Fe XVIII line ratio, which resembles optical line diagnostics often used in the HII region (e.g., Osterbrock and Ferland 2006).

One of the most significant contributions of the RGS data is to confirm the absence of O VII triplet (21–22 Å) in a few gas-rich elliptical galaxies (e.g., NGC 4472 and NGC 4636). Since they must be present in the X-ray spectra from the relatively cool gas (see Table 5.1), this strongly indicates that there is very little contribution from the gas below kT < 0.5 keV. A similar result was also reported in the cluster of galaxies and used to argue against the earlier cooling flow model predictions (e.g., Fabian et al. 2000; Sanders and Fabian 2010).

One may expect that the RGS spectra could provide the definite answer for the metal abundance problem, since individual lines can be resolved. However, the results obtained by analyzing RGS spectra suffer from a number of serious

limitations for an extended source. The main drawback of X-ray grating instruments is that there is no slit to isolate a spatial region of interest when the X-ray emission is extended as in the hot ISM of gas-rich elliptical galaxies (gas-poor galaxies do not provide enough s/n). The field of view of RGS is 1° in the dispersion direction and 5′ in the cross-dispersion direction. Therefore, it is quite a challenge to separate the space and energy both of which disperse X-rays along the dispersion direction. In other words, the line spread function critically depends on the spatial distribution of the X-ray emission, such that even if different emission lines can be separated, they are considerably broadened. To overcome this problem, Xu et al. (2002) performed extensive Monte Carlo simulations by assuming a 3-D β model for the electron density, $n_e \sim [1 + (r/rc)^2]^{-3\beta/2}$ and by allowing the gas temperature to monotonically increase with increasing radius near the center. Ji et al. (2009) assumed a 2-D β model for the azimuthally averaged surface brightness, $[1 + (r/rc)^2]^{-3\beta+1/2}$ and determined the parameters by using corresponding MOS images.

Another challenge in measuring abundances with RGS data is that the continuum level is hard to determine. While this can be a problem in analyzing CCD spectra (see Sect. 5.3), it is more serious with the RGS grating data, because the limited energy range (0.3–2.5 keV) of RGS does not allow for proper measurement of the hard emission from LMXBs and AGN (also possibly from the cosmic background). The contribution from the hard component must be provided independently, e.g., Ji et al. (2009) used MOS/PN data, but source extraction regions are not the same. A less serious, but still important problem in the continuum level is that the background cannot be determined locally in the same detector for most gas-rich galaxies (e.g., Ji et al. applied the template background). Therefore, the absolute abundances measured with the RGS data should be taken with caution. As described in Sect. 5.4.4 below, the relative abundance ratio is less seriously affected by the uncertainty in the continuum level.

5.4.4 Abundance Pattern

In addition to the absolute metallicity, the relative abundance ratio (see Fig. 5.11) is very useful to constrain the metal enrichment history by directly comparing with the chemical evolution models. In particular, the ratio of α-elements to *Fe* has been widely used to measure the relative importance of SN Ia and SN II, because of their different production yields in different timescales. See Nomoto et al. (1997a) and Iwamoto et al. (1999) for SN Ia yields and Woosley and Weaver (1995), Thielemann (1996), Nomoto et al. (1997b, 2006), and Kobayashi et al. (2006) for SN II yields (for more details see Pipino in this book.) In Table 5.3, the SN yields in units of $M_\odot$ (taken from Iwamoto et al. 1999) are listed in column 2 for SN II and in columns 3–4 for two commonly used SN Ia explosion models, slow deflagration (W7) and delayed detonation explosion (WDD1). Also listed in columns 5–7 are individual elements in number relative to Fe from SN II for convenient comparison with observationally measured abundance ratios. The Fe peak elements (e.g., Fe, Ni)

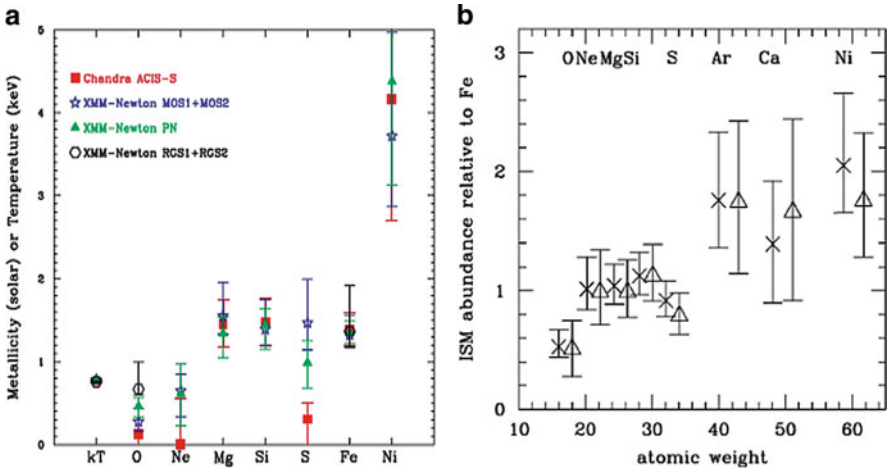

Fig. 5.11 (**a**) Abundances measured with the *XMM-Newton* and the *Chandra* observations of the central region ($r < 1'$) of NGC 4649 (top, taken from Ji et al. 2009). Elements heavier than Ne are modestly super-solar, while the two lighter metals, O and Ne, have abundances about a factor of 2 lower. (**b**) ISM abundance pattern (relative to Fe) in the inner (0–4′; *crosses*) and outer region (4′–8′; *triangles*) of NGC 4472, determined with Suzaku observations (Taken from Loewenstein and Davis 2010). Reproduced by permission of the AAS, see the electronic version for a color version of this figure

Table 5.3 SN yields

	In mass ($M_\odot$)			In relative number		
	SN II	SN Ia		SN II	SN Ia	
	10–50 $M_\odot$	W7	WDD1	10–50 $M_\odot$	W7	WDD1
O	1.80	1.43E-01	8.82E-02	69.521	5.511	3.399
Ne	2.31E-01	4.52E-03	1.45E-03	7.080	0.132	0.044
Mg	1.23E-01	8.57E-03	7.69E-03	3.100	0.220	0.197
Si	1.22E-01	1.57E-01	2.74E-01	2.669	3.445	6.022
S	4.12E-02	8.70E-02	1.63E-01	0.791	1.674	3.138
Ar	7.99E-03	1.57E-02	3.23E-02	0.136	0.267	0.553
Ca	5.87E-03	1.19E-02	3.10E-02	0.090	0.184	0.479
Fe	9.07E-02	7.49E-01	6.72E-01	1	8.280	7.422
Ni	5.97E-03	1.26E-01	3.81E-02	0.062	1.330	0.403

are mostly produced from SN Ia. Some α-elements (O, Ne, Mg) are predominantly produced from SN II and other α-elements (Si, S) are produced by both types in comparable proportions. Kobayashi et al. (2006) also considered hypernovae (HNe) which have significantly higher explosion energies than normal SNe II and have different yields for some heavy elements (e.g., Zn, Co, Mn). However, adding HNe to nomal SNe II does not significantly affect the abundance of those elements of interest (relative to Fe) listed in Table 5.3 (see also Nomoto et al. 2006).

It is important to note that the SN II yields significantly vary among different studies and that the uncertainties are not fully understood, e.g., the effect of mass loss and rotation in initially massive stars (see Gibson et al. 1997; Romano et al. 2010). The SN II yields can also vary, depending on the adopted IMF and progenitor pre-enrichment levels. For more details, see the above references. For SN Ia yields, the two SN Ia models predict quite different yields in most elements, except Fe. The differences for O, Ne and Mg are not important, because they are primarily produced in SNe II. Most notable are (1) the delayed detonation model produces higher yields for Si, S, Ar and Ca by a factor of ∼2 (see Sect. 5.4.5) and (2) the deflagration model produces higher yields for Ni by a factor of ∼3 (see 4.4.5). It seems that different observational data exclusively support the deflagration or delayed detonation model (Sects. 5.4.4.5 and 5.4.4.7). Among the delayed detonation models, WDD1, WDD2 and WDD3 in order of increasing density at DDT (deflagration to detonation transition) produce progressively less Si and S, but more Fe and Ni (see Iwamoto et al. 1999). In this chapter, we use two representative modes, W7 and WDD1.

Following the solar standard in Table 5.2, we convert the SN yields to abundance ratios relative to Fe in solar units in Table 5.4. They provide the abundance ratios when only one type of SNe dominates. We list the abundance pattern under three solar standards so that the reported results measured with different solar standards can be compared. In Table 5.5, we list an example set of the ISM abundance pattern in solar units, when individual elements from the SN Ia and SN II ejecta are linearly combined, assuming the number ratio of two types of SNe, N(SN Ia)/N(SN II) = 1/3. This ratio is selected to reproduce the solar Si/Fe abundance ratio, if we take the ASPL standard and the W7 SN II model. As described in Sect. 5.4.2 (and Sect. 5.4.4.1 below), the Si/Fe ratio is close to solar in typical giant gas-rich elliptical galaxies.

The real ISM abundance pattern may be more complex than expressed by the linear combination of two sets of SN yields due to mass loss from evolved stars with non-solar (α-element enhanced) abundances and various metal transport mechanisms throughout the ISM evolution which could add, remove and/or mix various chemical elements in different scales in different locations, e.g., by

Table 5.4 Abundance ratio (X/Fe) in solar units

	II only			Ia only					
	ANGR	GRSA	ASPL	ANGR		GRSA		ASPL	
				W7	WDD1	W7	WDD1	W7	WDD1
O	3.82	3.25	4.48	0.04	0.03	0.03	0.02	0.04	0.03
Ne	2.69	1.86	2.63	0.006	0.002	0.004	0.002	0.006	0.002
Mg	3.82	2.58	2.46	0.03	0.03	0.02	0.02	0.02	0.02
Si	3.52	2.52	2.60	0.55	1.07	0.39	0.77	0.41	0.79
S	2.29	1.17	1.89	0.58	1.22	0.30	0.62	0.48	1.01
Ar	1.74	1.72	1.72	0.41	0.96	0.41	0.94	0.41	0.94
Ca	1.84	1.25	1.30	0.45	1.32	0.31	0.90	0.32	0.94
Ni	1.63	1.11	1.17	4.23	1.43	2.87	0.97	3.03	1.02

Table 5.5 Abundance ratio (X/Fe) in solar units in case N(SNe Ia)/N(SNe II) = 1/3 by number

	ANGR		GRSA		ASPL	
	W7	WDD1	W7	WDD1	W7	WDD1
O	1.06	1.14	0.90	0.97	1.24	1.33
Ne	0.73	0.79	0.51	0.55	0.72	0.77
Mg	1.06	1.14	0.71	0.77	0.68	0.74
Si	1.35	1.79	0.97	1.28	1.00	1.32
S	1.04	1.53	0.53	0.78	0.86	1.27
Ar	0.77	1.19	0.76	1.17	0.76	1.17
Ca	0.83	1.47	0.56	1.00	0.59	1.04
Ni	3.53	1.49	2.39	1.01	2.53	1.07

partial/full winds, AGN-driven buoyant bubbles, infall (dilution by ICM), mergers, ram-pressure stripping, tidal stripping, metal depletion (in different degrees for different elements) etc. Nevertheless, all elements which we are discussing in this chapter had been formed in SNe, regardless of how they were recycled. Therefore, to the first approximation, Tables 5.4 and 5.5 provide a useful guideline to compare and interpret the observed abundance pattern. We refer readers to Pipino (in this book) for more complex mixing of elements, depending on galaxy evolution models.

It is also important to note that while the absolute abundance is seriously affected by the uncertainty of the continuum level, the relative abundance (or abundance ratio of two elements) is less affected by this problem. This can be understood by a correlation between errors in individual elements. In other words, the 2D confidence contours of two interesting parameters (e.g., Fe and Si) are often elongated diagonally. Because the abundance is determined by the line to continuum ratio, the uncertainties in the continuum level will affect both elements in the same manner, i.e., if one element is over-estimated, the other element is also overestimated and vice versa. The continuum may be affected by incorrect absorption (Sect. 5.3.2), incorrect subtraction of non-gas X-ray emission, such as LMXBs, ABs, CVs, AGNs and background (see Sect. 5.3.3), tying elements at incorrect solar ratios (Sect. 5.3.6), and helium sedimentation (3.10). Partly because of this, even if the absolute abundance is different in different studies, the relative abundance may be still consistent (e.g., compare Fig. 5.11a, b). Also the Si to Fe ratio is close to solar even if the absolute abundance is quite low in the early report (Sect. 5.4.1; also see Fig. 5.6a in Sect. 5.3.6).

Given that the measurement of elements other than Fe requires high s/n spectra, the abundance pattern is not easily measured in gas-poor elliptical galaxies. Therefore, the following results and related discussions are mainly for gas-rich galaxies.

5.4.4.1 Silicon

Among α-elements, Si is most useful and best measured, because of its strong, isolated emission features. The theoretical yield of Si is also the best determined,

with the least amount of scatter between model predictions (e.g., Gibson et al. 1997; Nagataki and Sato 1998). As shown in Table 5.4, it is expected that the Si/Fe abundance ratio is ∼2.5 solar, if heavy elements were mainly synthesized in SN II.

For example, significantly enhanced alpha to Fe ratios are seen in metal poor Galactic halo stars and local group dwarf galaxies with low Fe/H ratios which basically represent pure SN II products (e.g., see Pagel 2009). This ratio would decrease with increasing contributions from SN Ia. If the SN Ia contributed most of the hot ISM metals, the Si/Fe abundance ratio would be ∼0.5 solar (for W7). Typical giant elliptical galaxies have Si/Fe close to solar (see Fig. 5.11). Examples are NGC 1399 (Buote 2002), NGC 5044 (Buote et al. 2003), NGC 507 (Kim and Fabbiano 2004), NGC 7619 (Kim et al. 2008) and NGC 4472 (Loewenstein and Davis 2010). More examples can be found in the Chandra and XMM-Newton archival studies by Humphrey and Buote (2006) and Ji et al. (2009). The solar Si/Fe ratio indicates that the ejecta from both SNe II (from early star formation) and SNe Ia (continuously added later) are well mixed in these elliptical galaxies. With SN yields in Table 5.3, the measured solar abundance ratio of Si to Fe indicates that ∼70% of the detected iron mass was produced by SN Ia.

In contrast with the typical old elliptical galaxies, α-elements are significantly enriched in the ISM of merging galaxies where new stars are actively forming (e.g., in the Antennae, Fabbiano et al. 2004; Baldi et al. 2006). Kim (2010) found a signature of enhanced Si relative to Fe (i.e., super-solar Si/Fe ratio) in two young elliptical galaxies, NGC 720 and NGC 3923 by using deep Chandra observations and isolating the X-ray emission from the central 30". Figure 5.6 shows the relatively strong Si feature (at E ∼ 2 keV) from the central region of NGC 720 which can be compared with Fig. 5.5 for a typical case of the solar Si/Fe ratio (the 2 keV Si emission feature is less strong). This may indicate that the enhanced α-elements in young elliptical galaxies reflect the second generation star formation and additional SN II associated with recent major/minor mergers. However, other studies for the same galaxies, but with spectra extracted from a larger spatial region with XMM-Newton and Suzaku observations do not show this trend of enhanced α-elements (Ji et al. 2009; Tawara et al. 2008). Due to the low spatial resolution of XMM-Newton and Suzaku observations, multi-phase gas may be mixed in their spectra. This age effect needs to be confirmed with deep Chandra observations with a bigger sample of young elliptical galaxies.

5.4.4.2 Oxygen

The low O abundance (sub-solar O abundance as well as sub-solar O/Fe and O/Mg ratios) is unequivocally reported. The O to Fe ratio is ∼ 0.3 solar in NGC 5044, (Buote et al. 2003; David et al. 2010), 0.3–0.5 solar in NGC 507 (Kim and Fabbiano 2004) while the Mg to Fe ratio is only slightly lower than solar (0.8–0.9 solar) in both galaxies. Recent studies with the Chandra and XMM-Newton archival data by Humphrey and Buote (2006) and Ji et al. (2009) and with Suzaku data of NGC 4472 by Loewenstein and Davis (2010) also show the same trend: the O/Fe

ratio is ∼0.5 solar, while the Mg/Fe ratio is close to solar, resulting in the O/Mg ratio ∼0.5 solar (see Fig. 5.11). The above observed ratios were based on GRSA, except Humphrey and Buote (2006) who adopted an older version of ASPL. Both ratios would be higher by a factor of 1.4 when converted from GRSA to ASPL due to the lower O abundance in ASPL (see Table 5.2).

With a simple combination of SN II and SN Ia, for example, if the Si/Fe ratio is close to solar (Table 5.5), the O/Fe ratio would be 0.9–1.3 solar depending on the solar standard. Since both O and Mg are mainly produced by SN II, the O/Mg ratio does not depend on the SN Ia rate. Based on the SN II yield alone, the O/Mg ratio should be close to solar in ANGR and GRSA, or super-solar (1.8 solar) in ASPL, regardless of the Si/Fe ratio. Therefore, the observed ratios of O/Fe and O/Mg are clearly inconsistent with those expected from the SN yields. Possible explanations for this unexpected low O abundance include a warm absorber (Buote et al. 2003), Population III hypernovae (Humphrey and Buote 2006) and incorrect standard core collapse nucleosynthesis models which simply overproduce O by ∼2 (Ji et al. 2009; Loewenstein and Davis 2010).

The O abundance is also measured in the warm (∼10000 K) ionized gas by measuring the line ratios of O II and O III emission lines to H Balmer lines (Athey and Bregman 2009; Annibali et al. 2010). In general, early type galaxies contain only a small amount of the warm ISM (e.g., Kim 1989; Sarzi et al. 2007), if any, and those emission line galaxies are mostly LINERs. Using a small sample (mainly consisting of LINERs), Athey and Bregman (2009) and Annibali et al. (2010) reported that the O abundance in the warm ISM is close to or slightly lower than solar. Annibali et al. (2010) further reported that the gas O abundance is lower (by 0.2 dex) than that of stars and suggested the possibility of the incorrect O yield from SN II. However, note that the O abundance in the warm ISM depends on the ionization mechanism which is not fully understood yet for LINERs.

5.4.4.3 Neon

Similar to O and Mg, Ne is also primarily produced by SN II (Table 5.3) and the Ne to Mg ratio is expected to be close to solar, 0.7 solar in ANGR and GRSA, and 1.1 solar in ASPL (Tables 5.4 and 5.5). The reported Ne/Mg ratios vary from one galaxy to another. It is about a half solar in NGC 4649 and NGC 5044 (Ji et al. 2009), while close to solar in NGC 4636 (Xu et al. 2002; Ji et al. 2009) and NGC 4472 (Loewenstein and Davis 2010). See the contrast in Fig. 5.11a, b. Given the associated uncertainties, the Ne/Mg ratio may still be close to solar.

5.4.4.4 Magnesium

As described above, Mg is primarily produced by SN II (Table 5.3). The observed Mg to Fe ratio is close to solar in most galaxies (see Fig. 5.11). For example, the Mg/Fe ratios measured in 20 galaxies by Humphrey and Buote (2006) are all

consistent with solar. Combining SN II and SN Ia yields in Table 5.5, the Mg/Fe ratio would be 0.7–1.1 solar depending on the solar standard.

5.4.4.5 Nickel

The Ni/Fe ratio may be super-solar (1.5–3 solar) in NGC 1399, 4472, 4649 and 5044 (Ji et al. 2009; Loewenstein and Davis 2010). A similarly high Ni/Fe ratio is also found in the gas-rich galaxies by Humphrey and Buote (2006). Because both Ni and Fe are primarily produced in SN Ia (Table 5.3), the Ni/Fe ratio is useful to constrain the SN Ia model. In particular, the two SN Ia explosion models (deflagration and delayed detonation explosion) predict quite different Ni/Fe ratios. In the former model the Ni/Fe ratio ∼3 solar, while in the latter model the Ni/Fe ratio ∼1 solar (see Tables 5.4 and 5.5). The measured super solar Ni/Fe ratio seems to prefer the W7 model rather than WDD1 (see also Dupke and White 2000).

5.4.4.6 Other Elements (Sulfur, Argon, Calcium)

In term of SN yields, S, Ar and Ca are more or less similar to Si. The yields of the SN Ia deflagration model (W7 in Table 5.3) are higher by a factor of ∼2 than those of SNe II and the yields of the delayed detonation model (WDD1 in Table 5.2) are higher by another factor of ∼2 than the deflagration model. Taking the number ratio of two types of SNe, N(SN Ia)/N(SN II) = 1/3 (in Table 5.5), they are produced by both types of SNe in similar proportions. As expected, the S abundance measured in a few gas-rich galaxies with relatively hotter gas is more or less similar to the Si abundance, i.e., S/Fe ∼ solar (Fig. 5.11; see also Humphrey and Buote 2006; Ji et al. 2009). However, its error is large because the S emission lines are at higher energies and their peak temperature (1.5–2 keV in Table 5.1) is higher than the typical ISM temperature. Also note that the S lines are not observed by the RGS.

Ar and Ca are harder to measure, because they originate from even higher temperature gas (peak temperature = 2–4 keV in Table 5.1). Analyzing Suzaku X-ray spectra of NGC 4472 (Fig. 5.11b), Loewenstein and Davis (2010) found that the Ar and Ca abundances are similar (and super-solar), but with a large error. It is interesting to note that analyzing XMM-Newton data of a sample of 22 clusters of galaxies where Ar and Ca can be measured more reliably, de Plaa et al. (2007) found sub-solar Ar/Ca ratios in the central region ($0.2 \times R_{500} = 200$–400 kpc). They further discussed the quality of type Ia models and proposed a modified delayed detonation model based on Tycho SNR.

5.4.4.7 Comparison with Models

While the observed abundance pattern of the ISM and ICM has been extensively compared with model predictions, there is no simple combination of SNe yields

which can reproduce the observation abundance pattern (e.g., Gibson et al. 1997, 2007; Nagataki and Sato 1998; Pipino et al. 2005; for more discussions see also Pipino in this book). Loewenstein and Davis (2010) further compared the observed elemental abundance pattern with those predicted by simple chemical evolution models. In NGC 4472 (see Fig. 5.11b), they found that the best-fit temperatures in a 2-T model are 0.8 keV and 1.4 keV in $r < 2.5'$ and increase with increasing galactocentric distance (1 keV and 1.6 keV at $r = 5'$). As discussed in Sect. 5.4.2.1, the two temperatures are similar to those of NGC 507 and NGC 1399. The two phases likely represent the stellar system (the cooler one) and the group/cluster potential (the hotter one). It is likely that two phases of the ISM have different absolute and relative abundances. However, it is difficult to model two sets of abundance patterns, because they are not easily separated. They attempted to reproduce the observed abundance patterns with α-element enhanced stellar mass loss and a reduced SN Ia rate (by a factor of 4–6). Most elements could be reproduced, but still failed to match the entire observed pattern; for example, Ca and Ar (under-predicted) and O (over-predicted). With WDD1 yields (delayed detonation) instead of standard W7 yields, the observed pattern of Ca and Ar can be reproduced, but then S and Ni are over-predicted and under-predicted, respectively.

5.4.5 Spatial Variation of Metal Abundances

The radial profiles of elemental abundances and abundance ratios have direct implications on metal enrichment history by two types of SNe and metal transport mechanisms, e.g., by SN-driven global/partial winds and AGN-driven buoyant bubbles. Consequently, the radial abundance profiles have been extensively studied for clusters of galaxies (e.g., Mushotzky et al. 1978; Finoguenov et al. 2002; Tamura et al. 2004; Simionescu et al. 2009; see also a recent review by Bohringer and Werner 2010). However, this study in elliptical galaxies is limited only to gas-rich, cD type group dominant galaxies listed in Sect. 5.4.2.1, and the measurement error is still large at large radii due to the limited statistics.

As described in Sect. 5.4.2 (e.g., Fig. 5.8a), the Fe abundance generally decreases with increasing galacto-centric distance in gas-rich elliptical galaxies, e.g., NGC 507 (Kim and Fabbiano 2004) and NGC 1399 (Buote 2002). See also Buote (2000) for earlier ROSAT results. When azimuthally averaged, the Fe abundance is super-solar at the center and sub-solar (0.3–0.5 solar) at the outskirts. The latter is generally consistent with the typical ICM metal abundance (e.g., Mushotzky et al. 1978, 1996; Edge and Stewart 1991). Rasmussen and Ponman (2007) found a similar abundance gradient in a sample of galaxy groups. Johnson et al. (2009) also found a radial gradient in a gas-rich Virgo elliptical galaxy, NGC 4636. They further pointed out the effect of the abundance gradient on the mass measurement, because allowing the abundance gradient would result in a flat density profile and potentially reduce the gravitational mass.

While the Fe and Si abundances show radial variations, the Si to Fe abundance ratio appears to be constant, although a mild radial gradient, either positive or negative, cannot be ruled out due to the error at large radii (e.g., Fig. 5.8b). This roughly uniform Si/Fe ratio suggests that SN II and SN Ia ejecta are well mixed on a larger scale (∼100 kpc) than the optical galaxy (∼40 kpc). A similarly flat radial profile of the Si/Fe ratio has been found even in a larger scale (∼500 kpc) in galaxy clusters (e.g., Finoguenov et al. 2002; Tamura et al. 2004).

In contrast to Fe and Si, O is more or less uniformly distributed over the ICM, i.e., the O/Fe ratio has a positive radial gradient (e.g., Tamura et al. 2004). Although it is less clear in the ISM, because of a large error at the large radii (e.g., Buote et al. 2003; Kim and Fabbiano 2004; David et al. 2010), the under-abundant O (i.e., sub-solar O/Fe and O/Mg ratios) near the center of gas-rich elliptical galaxies (Sect. 5.4.4.2) is consistent with being flatter than Fe as in galaxy clusters.

As explained in Sect. 5.4.4, while Fe and O are exclusively produced by SN Ia and SN II respectively, Si is produced by both types of SNe. Through the early star formation episode in elliptical galaxies, the ISM would be primarily enriched by SN II and then ejected from host galaxies by SN-driven galactic winds. The SN II ejecta (e.g., O) would be distributed to large radii from the galaxy center and/or accumulated in the ICM. After the early star formation ended, the ISM in the passively evolving elliptical galaxies would be enriched by SN Ia ejecta, e.g., Fe which would be centrally peaked with a negative radial gradient. In this simple picture, the radial profile of Si (produced by both types of SNe) is expected to be flatter than that of Fe, but steeper than that of O. The Si/Fe ratio would increase with increasing distance up to ∼2 solar (close to the ratio given by SN II – Table 5.4) at large radii (e.g., Mushotzky et al. 1996). However, the observed radial profiles do not fit this simple picture. The flat Si/Fe profile may suggest the diversity of SNe Ia, i.e., both deflagration (producing lower Si yields, dominating earlier) and delayed detonation (producing higher Si yield, dominating later) scenarios are required (Finoguenov et al. 2002). Studying 6 clusters of galaxies, Simionescu et al. (2009) found that O is also centrally peaked, although less steep than Fe (still a positive O/Fe gradient), suggesting that the initial enrichment by SNe II in the early phase is not well mixed on large scales as previously thought.

It has been reported that while the metallicity decreases with increasing radius in a large scale, there may be a metallicity deficit in the very center of gas-rich galaxies (mostly cD-type galaxies). If real, this seems to be in contrast to what we expect by the metal enrichment from stellar ejecta. Examples are M87 (Gastaldello and Molendi 2002), the core of the Centaurus cluster (Sanders and Fabian 2002), NGC 5044 (Buote et al. 2003b) and a sample of galaxy groups (Rasmussen and Ponman 2007). Furthermore, using 3-D hydrodynamic simulations of hot gas in an intermediate mass galaxy, Tang and Wang (2010) showed that the positive metallicity gradient at the very center may be a natural consequence of a high outward velocity of hot SN ejecta due to the large buoyancy. If real, the resonance scattering (Sect. 5.3.7), the He sedimentation (Sect. 5.3.8), and the AGN feedback may also play a role. However, given that the central region is the most complex in thermal and chemical structures of the multi-phase hot ISM, this observational result may be caused by incorrect analysis, interpretation, and/or modeling. For example,

Buote et al. (2003b) showed that the abundance dip in the center of NGC 5044 disappeared when the abundances in each component of a 2T model are allowed to vary independently. With deep Chandra observations of the same galaxy, NGC 5044, David et al. (2010) showed that while the Fe abundance dip appears at the center ($r < 10$ kpc) if all elements are tied to Fe, it disappears if O is allowed to vary independently of Fe.

5.5 Summary

The morphological and thermal structures of the hot ISM in gas-rich elliptical galaxies are quite complex as seen in a few ultra deep Chandra observations (e.g., M87, NGC 5044). The hot ISM consists of multi-phases with various sub-structures related to AGN activities and interactions with the ambient medium. Consequently, the chemical structure of the hot ISM is also complex, when measured with spatially resolved spectroscopy, using a high spatial-resolution spectroscopic data.

In the gas-rich (cD and non-cD) galaxies, the Fe abundance is close to solar, or slightly super-solar in the central region. The early controversial report of the extremely sub-solar Fe abundance is now statistically excluded. The Si/Fe ratio is close to solar in typical giant old galaxies, as expected from a mixture of SN Ia and SN II ejecta. While the Mg/Fe ratio is close to solar, the O/Fe ratio is sub-solar, resulting in a sub-solar O/Mg ratio. Since both O and Mg are produced by SNe II, the observed O/Mg ratio is lower than expected. The solution of this problem is still unknown. Ni/Fe may be super-solar, favoring the deflagration model for SN Ia (however, other observational results prefer the delayed detonation model or mixture of both models). The entire abundance pattern is not reproduced by a simple combination of two SNe yields, or by a simple model with mass loss from stars with non-solar (α-element enhanced) abundances.

While gas-poor elliptical galaxies are more common than gas-rich elliptical galaxies, low s/n spectra result in large uncertainties in the ISM metal abundances in these galaxies, Consequently, the results are still controversial and the Fe abundance could be either sub-solar or close to solar. While the Fe abundance is expected to be close to solar as in gas-rich galaxies (at least similar to the stellar metallicity), the current observational data cannot fully reject the lower Fe abundance. The future generation of X-ray missions with high spatial and spectral resolution, e.g., Chandra spatial resolution combined with calorimeter spectral resolution, is critically required for the most accurate measurement of the metal abundances in the hot ISM in elliptical galaxies.

References

E. Anders, N. Grevesse, Geochimica et Cosmochimica Acta **53**, 197 (1989)
F. Annibali et al. 2010, A&A, **519**, A40
N. Arimoto et al., ApJ **477**, 128 (1997)

M. Arnaud, S. Majerowicz, D. Lumb et al., A&A **390**, 27 (2002)
M. Asplund, N. Grevesse, A.J. Sauval, P. Scott, ARA&A **47**, 481 (2009)
A.E. Athey, J.B. Bregman, ApJ **696**, 681 (2009)
H. Awaki et al., PASJ **46**, L65 (1994)
A. Baldi et al., ApJ **636**, 158 (2006)
A. Baldi et al., ApJ **707**, 1034 (2009)
M. Balucinska-Church, D. McCammon, ApJ **400**, 699 (1992)
B.A. Biller, C. Jones, W.R. Forman, R. Kraft, T. Ensslin, ApJ **613**, 238 (2004)
E.L. Blanton, C.L. Sarazin, J.A. Irwin, ApJ **552**, 106 (2001)
H. Bohringer, N. Werner, A&A Rev. **18**, 127 (2010)
B. Boroson, D.W. Kim, G. Fabbiano, 2011, ApJ, **729**, 12
D.A. Buote, C.R. Canizares, ApJ **427**, 86 (1994)
D.A. Buote, A.C. Fabian, MN **296**, 977 (1998)
D.A. Buote, ApJ **539**, 172 (2000)
D.A. Buote, ApJ **574**, L135 (2002)
D.A. Buote, A.D. Lewis, F. Brighenti, W.G. Mathews, ApJ **595**, 151 (2003a)
D.A. Buote, A.D. Lewis, F. Brighenti, W.G. Mathews, ApJ **594**, 741 (2003b)
A. Cardullo et al., A&A (2009)
Cash, ApJ **228**, 939 (1979)
P.A. Charles, F.D. Seward, *Exploring the X-ray Universe* (Cambridge University Press, Cambridge, 1995)
L. Ciotti, S. Pellegrini, A. Renzini, A. D'Ercole, ApJ **376**, 380 (1991)
L. Ciotti, S. Pellegrini, MNRAS **387**, 902 (2008)
L. David, C. Jones, W. Forman, P. Nulsen, J. Vrtilek, E. O'Sullivan, S. Giacintucci, S. Raychaudhury, ApJ **705**, 624 (2009)
L.P. David et al., 2011, ApJ, **728**, 162
D.S. Davis, R.E. White, ApJ **470**, L35 (1996)
J. de Plaa et al., A&A **465**, 345 (2007)
S. Diehl, T.S. Statler, ApJ **668**, 150 (2007)
S. Diehl, T.S. Statler, ApJ **687**, 986 (2008a)
S. Diehl, T.S. Statler, ApJ **680**, 897 (2008b)
R.A. Dupke, R.E. White III, ApJ **528**, 139 (2000)
A.C. Edge, G.C. Stewart, MNRAS **252**, 414 (1991)
S.C. Ellis, E. O'Sullivan, MNRAS **367**, 627 (2006)
S. Ettori & A.C. Fabian, MNRAS **369**, L42 (2006)
P. Eskridge, G. Fabbiano, D.W. Kim, ApJS **97**, 141 (1995)
G. Fabbiano, ARA&A **27**, 87 (1989)
Fabbiano et al., ApJ **605**, L21 (2004)
G. Fabbiano, D.W. Kim, G. Trinchieri, ApJ **429**, 94 (1994)
A.C. Fabian, J.E. Pringle, MNRAS **181**, 5 (1977)
A.C. Fabian et al., MNRAS **318**, L65 (2000)
A. Finoguenov, A. Matsushita, H. Bohringer, Y. Ikebe, M. Arnaud, A&A **381**, 21 (2002)
A. Finoguenov et al., ApJ **686**, 911 (2008)
F. Gastaldello, S. Molendi, ApJ **572**, 160 (2002)
N. Gehrels, ApJ **303**, 336 (1986)
B.K. Gibson, M. Loewenstein, R.F. Mushotzky, MN **290**, 623 (1997)
B.K. Gibson, P. S'anchez-Bl'azquez, , S. Courty, D. Kawata, in *Chemodynamics: From First Stars to Local Galaxies*, ed. by E. Emsellem et al. EAS Publications Series, vol. 24, p. 133 (also in astro-ph/061108, 2007)
M.R. Gilfanov, R.A. Syunyaev, Soviet Astron. Lett. **10**, 137 (1984)
O. Gonzalez-Martin et al., A&A **506**, 1107 (2009)
N. Grevesse, A.J. Sauval, Space Sci. Rev. **85**, 161 (1998)
M. Gudel, A&A Rev. **12**, 71 (2004)
P.J. Humphrey, D.A. Buote, ApJ **639**, 136 (2006)

P.J. Humphrey et al., ApJ **693**, 822–829 (2009)
J.A. Irwin, C.L. Sarazin, ApJ **471**, 683 (1996)
J.A. Irwin, C.L. Sarazin, J.N. Bregman, ApJ **570**, 152 (2002)
J.A. Irwin, A.E. Athey, J.N. Bregman, ApJ **587**, 356 (2003)
K. Iwamoto et al., ApJS **125**, 439–462 (1999)
J. Ji et al., 2009, ApJ **696** 2252
R. Johnson, D. Chakrabarty, E. O'Sullivan, S. Raychaudhury, ApJ **706**, 980 (2009)
J.S. Kaastra, *An X-Ray Spectral Code for Optically Thin Plasmas* (Internal SRON-Leiden Report, updated version 2.0) (1992)
D.W. Kim, ApJ **346**, 653 (1989)
D.W. Kim, Highlights Astron. **15**, 285 (2010)
D.W. Kim, G. Fabbiano, G. Trinchieri, ApJ **393**, 134 (1992)
D.W. Kim, G. Fabbiano, ApJ **441**, 182 (1995)
D.W. Kim, G. Fabbiano, H. Matsumoto, K. Koyama, G. Trinchieri, ApJ **468**, 175 (1996)
D.W. Kim, G. Fabbiano, G. Mackie, ApJ **497**, 699 (1998)
D.W. Kim, G. Fabbiano, ApJ **586**, 826 (2003)
D.W. Kim, G. Fabbiano, ApJ **613**, 93 (2004)
D.W. Kim, E. Kim, G. Fabbiano, G. Trinchieri, ApJ **688**, 931 (2008)
G.R. Knapp, E.L. Turner, P.E. Cunnifee, AJ **90**, 454 (1985)
G.R. Knapp, P. Guhathakurta, D.W. Kim, M. Jura, ApJS **70**, 329 (1989)
C. Kobayashi et al., ApJ **653**, 1145 (2006)
D.A. Liedahl, A.L. Osterheld, W.H. Goldstein, ApJL **438**, 115 (1995)
M. Loewenstein, W.G. Mathews, ApJ **373**, 445 (1991)
M. Loewenstein et al., ApJ **436**, L75 (1994)
M. Loewenstein, D.S. Davis, ApJ **716**, 384 (2010)
M. Machacek, C. Jones, W.R. Forman, P. Nulsen, ApJ **648**, 947 (2006)
H. Matsumoto et al., ApJ **482**, 133 (1997)
K. Matsushita, T. Ohashi, K. Makishima, PASJ **52**, 685 (2000)
R. Mewe, E.H.B.M. Gronenschild, G.H.J. van den Oord, A&AS **62**, 197 (1985)
R. Mewe, J.R. Lemen, G.H.J. van den Oord, A&AS **65**, 511 (1986)
E.T. Million et al., MNRAS **407**, 2046 (2010)
R. Morrison, D. McCammon, ApJ **270**, 119 (1983)
R.F. Mushotzky et al., ApJ **225**, 21 (1978)
R.F. Mushotzky et al., ApJ **436**, L79 (1994)
R.F. Mushotzky et al., ApJ **466**, 686 (1996)
S. Nagataki, K. Sato, ApJ **504**, 629 (1998)
J. Nevalainen L. David, M. Guainazzi, A&A (astro-ph/1008.2102) (2010)
K. Nomoto et al., Nuphy **621**, 467 (1997a)
K. Nomoto et al., Nuphy **616**, 79 (1997b)
K. Nomoto et al., Nuphy, **777**, 424 (2006)
D.E. Osterbrock, G.J. Ferland, *Astrophysics of Gaseous Nebulae and Active Galactic Nuclei* (University Science Books: Mill Valley, CA, 2006)
E. O'Sullivan, D.A. Forbes, T.J. Ponman, MNRAS **328**, 461 (2001)
E. O'Sullivan, T.J. Ponman, MNRAS **349**, 535 (2004a)
E. O'Sullivan, T.J. Ponman, MNRSA **354**, 935 (2004b)
B.E.J. Pagel, *Nucleosynthesis and Chemical Evolution of Galaxies* (Cambridge University Press, Cambridge UK, 2009)
S. Pellegrini, ApJ **717**, 640 (2010)
S. Pellegrini, G. Fabbiano, ApJ **429**, 105 (1994)
F. Peng, D. Nagai, ApJ **705**, L58 (2009)
A. Pipino, D. Kawata, B.K. Gibson, F. Matteucci, A&A **434**, 553 (2005)
P.P. Plucinski et al., in *SPIE Conference Series Vol. 7011: Space Telescopes and Instrumentation II: Ultraviolet to Gamma Ray* (2008)
F.V.N. Rangarajan, MNRAS **277**, 1047 (1995)

S.W. Randall, P. Nulsen, W.R. Forman et al., ApJ **688**, 208 (2008)
S.W. Randall et al., 2011, ApJ, 726, 86
J. Rasmussen, T. Ponman, J. MNRAS **380**, 1554 (2007)
J. Rasmussen, T. Ponman, J. MNRAS **399**, 239 (2009)
M. Revnivtsev, E. Churazov, S. Sazonov, W. Forman, C. Jones, A&A **473**, 783 (2007)
M. Revnivtsev, S. Sazonov, E. Churazov et al., Nature **458**, 1142 (2009)
E. Roediger, M. Bruggen, P. Rebusco, H. Bohringer, E. Churazov, MNRAS **375**, 15 (2007)
D. Romano, A.I. Karakas, M. Tosi, F. Matteucci, A&A, **522**, 32 (2010)
R.M. Sambruna, M. Gliozzi, D. Donato, F. Tavecchio, C.C. Cheung, R.F. Mushotzky, A&A, **414**, 885 (2004)
J.S. Sanders, A.C. Fabian, MNRAS submitted astro-ph/1012.0235 (2010)
C.L. Sarazin, J.A. Irwin, J.N. Bregman, ApJ **556**, 533 (2001)
M. Sarzi et al., NewAR **51**, 18 (2007)
F. Seward, in *Astrophysical Quantities* 4th edn., ed. by Cox. (AIP Press, New York, 2000)
A. Siemiginowska, *X-ray Astronomy Handbook*, ed. by K. Arnaud, R. Smith, A. Siemiginowska (Cambridge University Press, Cambridge, UK, 2011)
A. Simionescu, N. Werner, H. Böhringer, J.S. Kaastra, A. Finoguenov, M. Brüggen, P.E.J. Nulsen, A&A **493**, 409 (2009)
G.R. Sivakoff, C.L. Sarazin, J.A. Irwin, ApJ **599**, 218 (2003)
R.K. Smith, N.S. Brickhouse, D.A. Liedahl, J.C. Raymond, in *Spectroscopic Challenges of Photoionized Plasmas, ASP Conference Series*, ed. by G. Ferland, D.W. Savin, vol. 247 (Astronomical Society of the Pacific, San Francisco, 2001), p. 159
T. Tamura, J.S. Kaastra, J.W.A. den Herder, J.A.M. Bleeker, J.R. Peterson, A&A **420**, 135 (2004)
S. Tang, Q.D. Wang, MNRAS **408**, 1011 (2010)
Y. Tawara et al., PASJ **60**, 307 (2008)
F.K. Thielemann, , ApJ **460**, 408 (1996)
G. Trinchieri, D.W. Kim, G. Fabbiano, C.R. Canizares, ApJ **428**, 555 (1994)
G. Trinchieri, G. Fabbiano, D.W. Kim, A&A **318**, 361 (1997)
M. Tsujimoto et al., 2011, A&A, **525**, 25
N. Werner et al., MNRAS **398**, 23 (2009)
N. Werner et al., MMRAS **40**, 2063 (2010)
R.E. White III, C.L. Sarazin, ApJ **367**, 476 (1991)
J. Wilms, A. Allen, R. McCray, ApJ **542**, 914 (2000)
S.E. Woosley, T.A. Weaver, ApJS **101**, 181 (1995)
H. Xu et al., ApJ **579**, 699 (2002)